NASA Contractor Report 180845

Theoretical Analysis of the Electrical Aspects of the Basic Electro-Impulse Problem in Aircraft De-Icing Applications

Robert A. Henderson and Robert L. Schrag
Wichita State University
Wichita, Kansas

November 1987

Prepared for
Lewis Research Center
Under Grant NAG3-284

National Aeronautics and
Space Administration

Preface

This report is a part of the research and development project on aircraft de-icing by the electromagnetic impulse method. This project has been sponsored by the Lewis Research Center of the National Aeronautics and Space Administration under grant number NAG-3-284. The grant administrators were Mr. John J. Reinmann and Dr. R. Joseph Shaw. For the previous five years, many tests had been run in the NASA Icing Research Tunnel and three sets of flight tests were performed. These, plus various laboratory tests, have resulted in a semi-empirical technology for designing an electro-impulse de-icing (EIDI) system.

However, the empirical method is inadequate when a very different geometry, material or size is encountered. A computative solution is needed which permits prediction of the de-icing effect for a given configuration and electrical circuitry. This report, which is principally the Ph.D. dissertation of Robert A Henderson under the direction of Prof. Robert L. Schrag, attempts to do the first part of a full computer simulation of EIDI. The pressure/time produced by the method in the report would be necessary input for a computer code giving the structural dynamic response of a given configuration. The configurations in mind are leading edge portions of aircraft wings, engine nacelle inlets and rotor blades. Applications, however, are not limited to these uses.

The authors acknowledge the assistance of NASA-Lewis Research Center, both for the support of the whole EIDI project at Wichita State University and for the opportunity for Dr. Henderson to work at NASA-Lewis during the summers of 1985 and 1986. The assistance of Drs. R. Joseph Shaw, Bill Ford and Avram Sidi during that time is gratefully expressed.

TABLE OF CONTENTS

CHAPTER ONE

INTRODUCTION

1.1 ELECTRO-IMPULSE PHENOMENON AND DE-ICING

In a paper presented January 8, 1986, at the 24th AIAA Aerospace Sciences Meeting in Reno, Nevada, [1] author R. D. Rudich cited aircraft icing as the direct cause of four of the thirty two weather related fatal accidents reported in the paper. While this may not seem like a significant number, the loss of human lives in these four accidents could have been prevented if the aircraft involved had been able to cope with the icing conditions they encountered.

The purpose of this report is to present methods of analyzing the electromagnetic aspects of a new method of de-icing both private and commercial aircraft. This new de-icing method, referred to as Electro Impulse De-Icing (abbreviated EIDI), holds the promise of being superior to present aircraft de-icing methods in terms of the energy expended in removing accreted ice [42].

The EIDI concept is not new. In May 1939, Great Britain issued a patent to Mr. Rudolf Goldschmidt covering the basic EIDI mechanism [2]. However, no commercial development of an EIDI system in the free world proceeded from this patent. It has only been within the last 5 years that the unavailability of bleed air from the high bypass ratio engines used on the next generation commercial aircraft has caused attention to be directed to the use of an EIDI system for removing ice.

The simplest practical EIDI system consists of a spirally wound coil of rectangular cross section conductor mounted with its axis of symmetry

perpendicular to the metal surface to be de-iced. An initially charged capacitor is discharged through this coil, and the resulting magnetic field from the coil's current causes eddy currents in the metal. The force exerted on these eddy currents by the coil's magnetic field is initially in such a direction as to cause the coil and the metal surface to separate. It is this force that causes ice on the metal surface to crack, and subsequently to be removed from the surface.

A considerable body of literature concerned with the electromagnetic aspects of a coil placed next to a conducting surface has accumulated. Levy [8] and Grover [9] present methods of calculating terminal impedances. Dodd and Deeds [10] discuss both impedance calculations and eddy current distributions. Onoe [11] is apparently the first researcher to apply a Hankel transformation in the calculation of impedances. Onoe's method is further developed and extended by El-Markabi and Freeman [4] to include calculation of the force between the coil and conductor when the coil current is a sinusoid. Bowley et. al. [43] discuss the use of the magnetic vector potential in calculating the impulse delivered to the conductor by a single cycle of exponentially damped sine wave current in the coil. Lewis [44] summarizes the use of the Bowley method for designing a coil to deliver a specific impulse in an electro-impulse de-icing installation.

1.2 SCOPE OF REPORT

An experimental set-up of a prototype EIDI system was assembled at The Wichita State University by Dr. Robert Schrag. An experimental study of the electro-impulse phenomenon in this system was made by Dr. Schrag utilizing field diagnostics methods [3]. Axial and radial components of

the magnetic field were measured on both sides of the rigidly held aluminum "target" plate. The data were then used to deduce the total mechanical force versus time, and the mechanical impulse strength. Impulse strength was also measured directly with a ballistic pendulum. This experimental study provided results which will be used to verify theoretical predictions from the mathematical model used in this report.

In this report, the physical phenomena involved in the prototype EIDI system of Dr. Schrag's experiment will be investigated analytically and numerically. Specifically, the following tasks will be undertaken.

1. A mathematical model for the total electrical problem will be devised. It will employ a transmission line analogy to handle the electromagnetic field portion of the system, and a frequency domain model for the circuit portion.

2. The math model will be solved by computer for the specific set of conditions that existed in Dr. Schrag's diagnostics experiment, and the calculated and experimental results will be compared.

1.3 ORGANIZATION OF REPORT

Figure 1 summarizes the analysis structure developed in this report to predict the behavior of the prototype EIDI system briefly described in Section 1.1. Each of the blocks in this figure represents a stage in the procedure for determining the force-time profile on a rigid coil placed next to a fixed conducting plate (the "target") when a capacitor is discharged through the coil.

In Block 1 of Figure 1, Maxwell's equations are written for the coil and metal target of the physical system. A simple model of the coil that stresses the geometrical symmetry of the system is proposed , eliminating

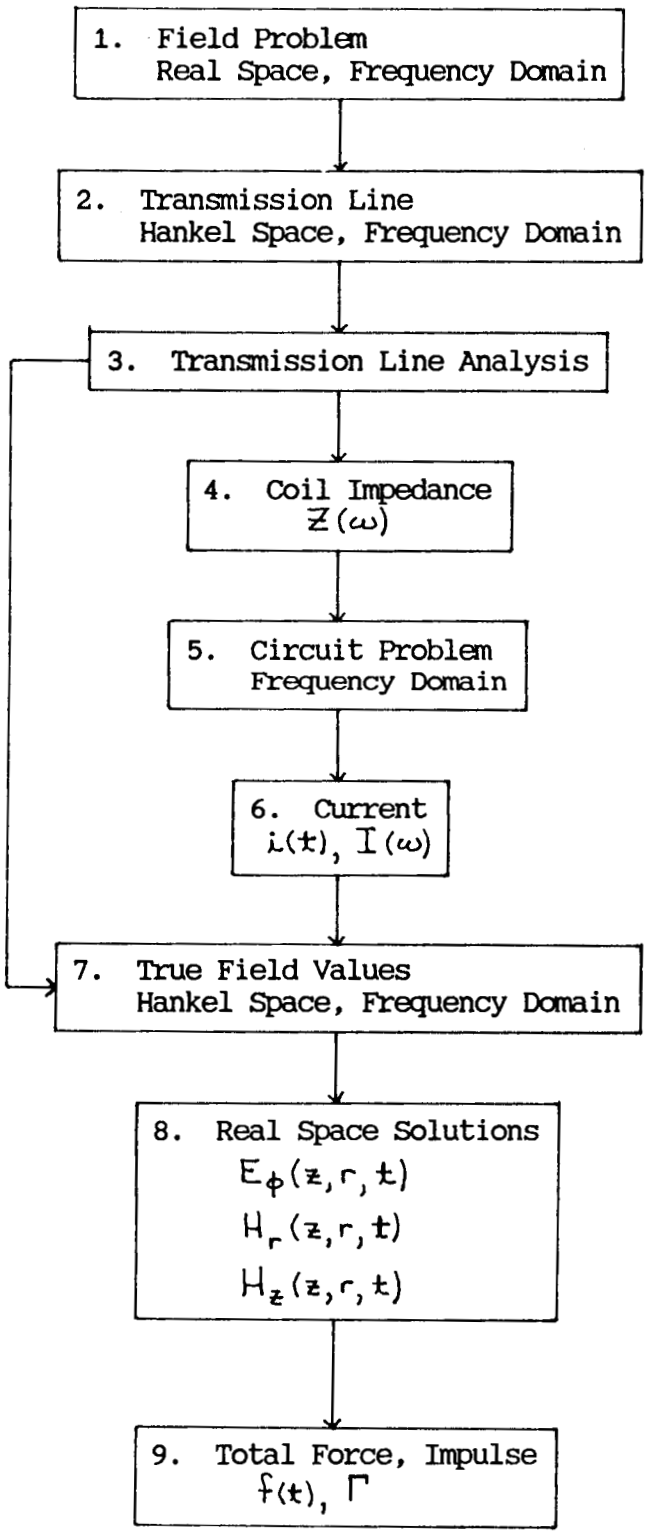

FIGURE 1
Analysis Flow Diagram

several terms from the Maxwell equations. Chapter 3 discusses this modeling of the coil and metal target, and shows that application of Fourier and Hankel transforms to the model equations results in a conceptual replacement of the field problem with an infinite set of transmission line problems (Block 2).

In Block 3 of Figure 1, the analysis of the transmission line model is performed. The methods of this analysis, for steady state sinusoidal conditions, may be found in Chapter 4. Chapters 3 and 4 provide the basic theoretical developments, with the results of the analyses in Chapter 4 applied in Chapter 6 to Dr. Schrag's prototype experimental EIDI system, described in Chapter 5. Modeling of the circuit used to provide energy to the coil is discussed in Chapter 2 for the specific experimental system of Chapter 5.

Once the transmission line model of the coil and target has been established in Block 3, Figure 1 shows two possible next steps in the analysis. One of these next steps, calculation of the true field values (Block 7), requires a knowledge of the coil current. Accordingly, one proceeds from the transmission line analysis in Block 3 to the Block 4 calculation of the coil impedance, required for calculating the coil current. Use of the transmission line model for calculating the part of the impedance of the coil that is due to the interaction between the coil and target is discussed theoretically in Section 4.2 of Chapter 4, and applied to the impedance calculation of the coil in the prototype EIDI system in Section 6.2 of Chapter 6.

Coil impedance obtained in Block 4 is added to the calculated skin effect loss resistance in the coil. With this total coil impedance, the problem of calculating coil current, using the circuit models presented

in Chapter 2, is addressed. This is Block 5, discussed in Section 6.3 of Chapter 6 for the prototype EIDI system described in Chapter 5.

Knowledge of the frequency spectrum of the coil current allows the calculation of the true field values in Hankel-Fourier space, shown in Block 7 and developed theoretically in Section 4.3 of Chapter 4. Performing an inverse Hankel transformation on these fields results in Fourier space fields. An inverse discrete Fourier transform applied to the Fourier space fields provides the time domain behavior of the electric and magnetic fields, shown in Block 8. This procedure is discussed in Section 6.4 of Chapter 6 for the prototype EIDI system.

Finally, the real space axial and radial magnetic induction fields on the coil side face of the metal target provide the necessary information for calculating the total force on the target as a function of time, as shown in Block 9. Development of the force equation is in Section 4.5 of Chapter 4, with Section 6.5 of Chapter 6 describing the numerical implementation of this force calculation for the prototype EIDI system. Calculation of the impulse delivered to the target is discussed theoretically in Section 4.6 of Chapter 4, and its application to the prototype EIDI system is described in Section 6.6 of Chapter 6.

Chapter 7 contains a summary of the results obtained, and some suggestions for improving the procedures for modeling the electrical aspects of an EIDI system described in this report.

A magnetic tape listing of the FORTRAN algorithms developed during the research described in this report are available at a nominal charge from the authors, at the address below.

Department of Electrical Engineering
The Wichita State University, Box 44
Wichita, Kansas 67208

CHAPTER TWO

THE ELECIRIC CIRCUIT MODEL

Modeling of the circuit providing power to the de-icing coil in an EIDI system is performed with the desired output from the model in mind. Since it is the coil current in conjunction with the physical configuration of the coil and metal target that determines the magnetic fields responsible for the forces on the target, the current in the circuit was chosen as the primary variable.

Testing of a prototype EIDI system began at The Wichita State University in 1982. The part of this system that provides power to the coil is shown in Figure 5 (page 34). This system was chosen as the basic physical configuration for which a circuit model would be derived. The circuit model is then analyzed to determine the coil current. A simple circuit model that is suggested by the physical system in Figure 5 is shown in Figure 17 (page 46). This is the basic circuit model, valid when the clamp diode across the capacitor is not conducting.

Justification for modeling the EIDI system as a lumped parameter circuit was provided by the experimental verification of the absence in the signals present of any significant frequency components having wavelengths comparable to the physical dimensions of the system. Because of the complex electromagnetic interaction between the coil and the target, it was felt that a time domain model of the coil's terminal v-i characteristics would be too complex to be of much use. Consequently, a frequency domain approach was chosen for analyzing the circuit, making the model of the coil a linear frequency dependent impedance.

The presence of the SCR and the clamp diode across the capacitor makes the circuit nonlinear, so that straightforward Fourier (frequency domain) techniques are not applicable. This difficulty is circumvented by performing a piecewise linear analysis of the circuit. In this analysis, the physical circuit is modeled by one of two possible circuits, depending on the state of the clamp diode. Initially, when the SCR has just been triggered, the diode is assumed off (an open circuit) and the model of Figure 17 (page 46) is used for analysis. Both the current and the capacitor voltage in this circuit are calculated. When the capacitor voltage first becomes negative, the clamp diode paralleling the capacitor is modeled as coming into immediate forward conduction. The diode then acts as a short circuit, resulting in the circuit model shown in Figure 18 (page 49). All subsequent (in time) circuit calculations are performed using this model.

Theoretical justification for modeling both the SCR and the clamp diode as simple on-off switches is now provided. However, the ultimate justification for such an outright dismissal of the effects of both the SCR and the clamp diode in determining the coil current comes from observing how closely the predicted current (using the models that ignore the non-ideal nature of the SCR and diode) agrees with the measured current. This will be shown in Chapter 6.

In a practical EIDI system, the voltage on the energy storage capacitor prior to its discharge is 1000 to 1500 volts. When the SCR is triggered into conduction, its voltage drop is on the order of 1 volt, which is small compared to the capacitor voltage, and so may be ignored in determining the circuit current. In addition to ignoring the voltage drop across the SCR, the dynamics of the SCR are also not modeled. Such

dynamics are, in the EIDI circuit, primarily manifested in the failure of the SCR to trigger into instantaneous full forward conduction upon application of a forward gate current. However, modern SCR design techniques [5], [6], [7] have resulted in turn-on times that are short compared to the time required for a significant change in the coil current in the experimental EIDI prototype system. The SCR used in the prototype system had a di/dt rating of 800 amps/microsecond, while the maximum observed rate of change of current in the circuit was 15 amps/microsecond.

A similar consideration of the voltage levels in the circuit results in the conclusion that the approximately 1 volt forward drop across the clamp diode is not a primary factor in determining circuit current. When the diode is off, its transition capacitance is insignificant compared to the 600 microfarad capacitance of the energy storage capacitor in parallel with it. Reverse leakage current in the diode is ignored due to this large energy storage capacitor and the relatively small time in which the electrical events of interest take place in the circuit. With the diode in forward conduction, the sum of its transition and diffusion capacitances are small enough that they also may be ignored in the circuit model.

In constructing the EIDI prototype experiment configuration, care was exercised to minimize parasitics in the circuit. Special low inductance and resistance cable was used to connect the energy storage capacitor to the coil. However, both of these cable parameters were measured in the prototype system and are taken into account in the circuit model. The energy storage capacitor, which was physically several capacitors in parallel, used copper strap for wiring connections to minimize inductance and resistance parasitics. The equivalent series resistance and equivalent series inductance of the capacitors were felt to be small, and are

not modeled. If, in a particular EIDI installation, these parasitics are not small, they may be taken into account by adding lumped elements in series with the energy storage capacitor in the circuit model.

Accurate frequency domain modeling of the coil is the most difficult feat in constructing the circuit model, and is discussed in Chapter 4.

CHAPTER THREE

TRANSMISSION LINE MODEL OF THE FIELD PROBLEM

3.1 INTRODUCTION

The transmission line model of the coil and metal target is the heart of the prototype EIDI system model. It is this model that is expected to account for the complex electromagnetic interactions between the coil and target. These interactions help establish the impedance presented at the coil terminals, and so are a factor in determining the coil current. This current is important in determining the force on the target.

3.2 GEOMETRY OF A PROTOTYPE EIDI SYSTEM

Figure 2 shows the profile of the physical coil-metal plate con-

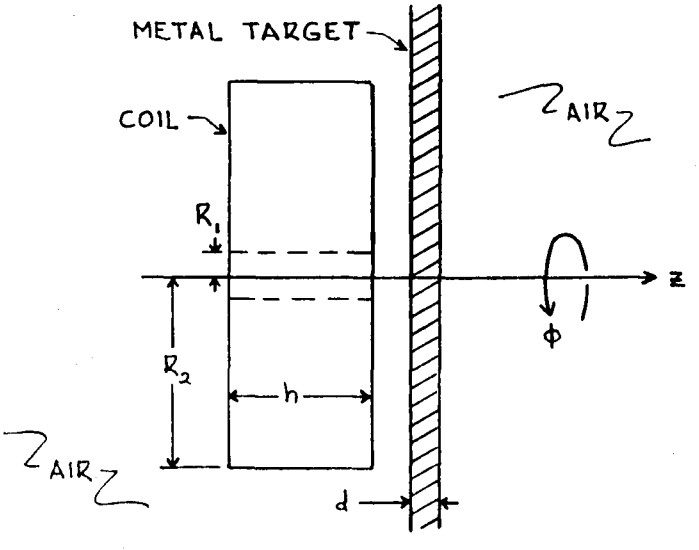

FIGURE 2
COIL-TARGET
GEOMETRY

figuration to be modeled. The coil has the shape of a short ($h<<R_2$) thick walled ($R_1<<R_2$) hollow cylinder with an inside radius R_1 and an outside radius R_2, whose axis is perpendicular to a flat metal target of

thickness d extending to infinity in all radial directions. An air gap exists between the coil and target, both of which are assumed rigid and stationary in space.

Most of the coils used in EIDI applications have been round, at least prior to a possible bending of the coil to conform to the curved leading edge of a wing. The flat geometry of Figure 2 is a reasonable model of such a coil, provided that the radius of curvature of the coil, after being shaped to conform to the wing, is much greater than the coil outer radius R_2.

The assumption that the coil and target remain separated by a fixed distance would be reasonable if the initial separation distance was much larger than the maximum change in separation distance obtained when the capacitor is discharged through the coil. Such an inequality in separation distances may not hold in a practical EIDI installation. Alternatively, the fixed separation distance assumption would be justified if the force "impulse" delivered to the plate by the coil was so short that the plate acquired only a small velocity, with negligible displacement, for the duration of the "impulse". This does not generally happen in a practical EIDI system. In fact, a well designed installation has the target move from zero to maximum displacement within the duration of the "impulse". With ice loading present, however, the displacement may be small compared to the initial separation distance.

3.3 THE FIELD EQUATIONS

The approach chosen for modeling the coil and target in the prototype EIDI system is presented in a paper by El-Markabi and Freeman [4]. This approach is now described, emphasizing those aspects of the theory

that are most appropriate to the analysis of the model of the prototype system of Figure 2. The reader is referred to El-Markabi and Freeman [4] for the more general theory.

Current in the coil of Figure 2 is assumed to be entirely phi directed. A slight modeling error is introduced by this assumption, since a radial component of current actually exists in a practical coil due to the spiral winding of the ribbon conductor. By neglecting this small radial current, a model having azimuthal symmetry is obtained. Consequently, the model shows no phi dependence in any of the field quantities, the electric field contains only a phi component, and the magnetic field contains only axial and radial components.

Because most of the spectral energy of the current in a practical EIDI coil is confined to relatively low frequencies, a quasi-static situation is assumed. The displacement current term in Ampere's Law is ignored.

With these assumptions, Maxwell's equations written for Figure 2 become

$$\frac{\partial E_\phi(z,r,t)}{\partial z} = \mu \frac{\partial H_r(z,r,t)}{\partial t}$$

$$\frac{1}{r}\frac{\partial}{\partial r}\left[r E_\phi(z,r,t)\right] = -\mu \frac{\partial H_z(z,r,t)}{\partial t}$$

$$\frac{\partial H_r(z,r,t)}{\partial z} - \frac{\partial H_z(z,r,t)}{\partial r} = \sigma E_\phi(z,r,t)$$

Partial differentiation with respect to time can be eliminated from these equations by taking the Fourier transform. Differentiation with respect to time is then replaced with multiplication by the $j\omega$ operator. Performing this transformation leads to the following equations (note that new symbols have not been introduced for the transformed field quantities;

instead, their time variable argument t has simply been replaced with the Fourier transform variable omega)

$$\frac{\partial E_\phi(z,r,\omega)}{\partial z} = j\omega\mu H_r(z,r,\omega) \tag{1}$$

$$\frac{1}{r}\frac{\partial}{\partial r}\left[r E_\phi(z,r,\omega)\right] = -j\omega\mu H_z(z,r,\omega) \tag{2}$$

$$\frac{\partial H_r(z,r,\omega)}{\partial z} - \frac{\partial H_z(z,r,\omega)}{\partial r} = \sigma E_\phi(z,r,\omega) \tag{3}$$

Equation (1) contains only the phi component of E and the radial component of H. By combining equations (2) and (3) in such a fashion as to eliminate the axial component of H, another equation containing only the phi component of E and the radial component of H results. This elimination yields

$$\frac{\partial H_r}{\partial z} = \sigma E_\phi + \frac{\partial H_z}{\partial r} = \sigma E_\phi + \frac{\partial}{\partial r}\left[\frac{-1}{j\omega\mu}\frac{1}{r}\frac{\partial}{\partial r}(rE_\phi)\right]$$

$$\frac{\partial H_r}{\partial z} = \sigma E_\phi - \frac{1}{j\omega\mu}\frac{\partial}{\partial r}\left[\frac{1}{r}\frac{\partial}{\partial r}(rE_\phi)\right] \tag{4}$$

At this point, a mathematical tool that is of considerable importance is introduced. This tool is the Hankel transform of order n, defined in [12] as

$$\mathcal{H}\{f(r)\} \triangleq \int_0^\infty f(r)\, r\, J_n(\lambda r)\, dr = F(\lambda)$$

with the inverse transform

$$\mathcal{H}^{-1}\{F(\lambda)\} = \int_0^\infty F(\lambda)\, \lambda\, J_n(\lambda r)\, d\lambda = f(r)$$

Although the use of an additional transform introduces difficulties of its own, it provides an even greater amount of simplification, and makes possible the transmission line model of the coil-target electromagnetic field problem.

If a Hankel transform of order 1 is applied with respect to the

variable r in equation (4), the following result is obtained [11], [12]. Note that new symbols have again not been introduced for the transformed quantities; instead, the spatial variable argument r has been replaced with the Hankel transform variable lambda.

$$\frac{\partial H_r(z,\lambda,\omega)}{\partial z} = \left(\sigma + \frac{\lambda^2}{j\omega\mu}\right) E_\phi(z,\lambda,\omega) \tag{5}$$

The advantage of equation (5) over equation (4) is that equation (5) contains partial derivatives with respect to only the z coordinate, in effect becoming an ordinary differential equation (if one allows "constants of integration" for such an equation to be arbitrary functions of all variables except z). If the same Hankel transform is applied to equation (1),

$$\frac{\partial E_\phi(z,\lambda,\omega)}{\partial z} = j\omega\mu H_r(z,\lambda,\omega) \tag{6}$$

Equations (5) and (6) are two coupled ordinary differential equations that are recognizable as the canonical transmission line equations. The solutions of these equations are well known [13], [14], [15].

3.4 DEVELOPMENT OF THE TRANSMISSION LINE MODEL

Because equations (5) and (6) are identical in form to the equations describing voltage and current on an ordinary transmission line, symbols V and I (each of which is a function of position z along the coil axis, the Fourier variable omega, and the Hankel variable lambda) are now introduced to represent the phi component of E and the radial component of H respectively. Then equations (5) and (6) become

$$\frac{\partial \hat{I}}{\partial z} = \left(\sigma + \frac{\lambda^2}{j\omega\mu}\right) \hat{V} \tag{7}$$

$$\frac{\partial \hat{V}}{\partial z} = j\omega\mu \hat{I} \tag{8}$$

Differentiating equation (7) with respect to z,

$$\frac{\partial^2 \hat{I}}{\partial z^2} = \left(\sigma + \frac{\lambda^2}{j\omega\mu}\right) \frac{\partial \hat{V}}{\partial z}$$

Substitution of equation (8) into this last equation yields

$$\frac{\partial^2 \hat{I}}{\partial z^2} = j\omega\mu \left(\sigma + \frac{\lambda^2}{j\omega\mu}\right) \hat{I}$$

$$\frac{\partial^2 \hat{I}}{\partial z^2} = \left(\lambda^2 + j\omega\mu\sigma\right) \hat{I} \tag{9}$$

Similarly, differentiate equation (8) to obtain

$$\frac{\partial^2 \hat{V}}{\partial z^2} = j\omega\mu \frac{\partial \hat{I}}{\partial z}$$

Substitution of equation (7) into this equation yields

$$\frac{\partial^2 \hat{V}}{\partial z^2} = j\omega\mu \left(\sigma + \frac{\lambda^2}{j\omega\mu}\right) \hat{V}$$

$$\frac{\partial^2 \hat{V}}{\partial z} = \left(\lambda^2 + j\omega\mu\sigma\right) \hat{V} \tag{10}$$

Now define the complex propagation constant gamma in Fourier-Hankel space as

$$\gamma = \sqrt{\lambda^2 + j\omega\mu\sigma}$$

so that the general solutions to equations (9) and (10), assuming complex sinusoidal time variation of $\hat{V}$ and $\hat{I}$, may be written as

$$\hat{I} = \hat{I}_{o+} e^{-\gamma z} + \hat{I}_{o-} e^{\gamma z} \tag{11}$$

$$\hat{V} = \hat{V}_{o+} e^{-\gamma z} + \hat{V}_{o-} e^{\gamma z} \tag{12}$$

where $\hat{I}_{0+}$, $\hat{I}_{0-}$ and $\hat{V}_{0+}$, $\hat{V}_{0-}$ are complex phasor functions of the Hankel variable lambda (the complex sinusoidal time variation has been suppressed in these solutions).

Note that there are an uncountably infinite set of transmission lines in the Hankel space model. Each transmission line is associated with a different value of lambda, with lambda real and non-negative. The physical origin of this infinite number of transmission lines lies in having "compressed" the infinite radial variation in the real space field quantities H_r and E_ϕ at a given axial coordinate z into variables V and I localized to a single "point" (the corresponding z coordinate) on a Hankel space transmission line. It then takes an infinite number of transmission lines to account for the infinite number of possible values of the radius in the real space problem.

To derive an expression for the characteristic impedance of one of these Hankel space transmission lines, consider the case of a line having only a single frequency complex sinusoid traveling in the direction of increasing z. In agreement with ordinary transmission line theory, the negative sign in the exponents in equations (11) and (12) denotes propagation in the direction of increasing z. Then equations (11) and (12) become

$$\hat{I} = \hat{I}_{o+} e^{-\gamma z} \tag{13}$$

$$\hat{V} = \hat{V}_{o+} e^{-\gamma z} \tag{14}$$

Substitute the expressions for the current and voltage from equations (13) and (14) into equation (7)

$$-\hat{I}_{o+} \gamma e^{-\gamma z} = (\sigma + \frac{\lambda^2}{j\omega\mu}) \hat{V}_{o+} e^{-\gamma z}$$

From this equation, the defining expression for the characteristic impedance of a Hankel space transmission line is obtained as

$$Z_o \triangleq \frac{\hat{V}_{o+}}{\hat{I}_{o+}} = \frac{-\gamma}{\sigma + \frac{\lambda^2}{j\omega\mu}}$$

$$Z_o = \frac{-j\omega\mu}{\sqrt{\lambda^2 + j\omega\mu\sigma}}$$

This result differs by a negative sign from the expression given in El-Markabi and Freeman [4] for the line's characteristic impedance. One could argue that the negative branch of the square root function in the expression for the propagation coefficient gamma should be chosen, which would eliminate the negative sign in the characteristic impedance. However, calculations performed with a negative characteristic impedance result in predictions that are essentially in agreement with experimental measurements, whereas the use of a positive characteristic impedance predicts results that are not in agreement with experiment. Alternatively, one could propose that it is the positive sign that must be chosen for the exponents in equations (11) and (12) to correspond to propagation in the direction of increasing z. Such an assumption also results in predictions that are not in agreement with experiment.

Transformation of real space current sources into Hankel space is discussed in El-Markabi and Freeman [4]. They show that a disc of azimuthally directed uniform surface current of phasor value $\tilde{I}$, with an inner radius R_1 and an outer radius R_2, located on the z-axis, becomes a sinusoidal current source with phasor value

$$\frac{\tilde{I}}{R_2 - R_1} \int_{R_1}^{R_2} r J_1(\lambda r)\, dr$$

connected in parallel with the Hankel space transmission line. The z coordinate of this current source is the same as the z coordinate of the real space surface current from which it arose.

Three of these ideal azimuthally directed discs of uniform surface current have been chosen to model the current distribution in the coil. The inner (outer) radius of the disc is equal to the inner (outer) radius of the coil. The middle disc is located at the axial center of the coil, while the two outer discs are each spaced out a distance of one-third of the coil's width from the center of the coil. See Figure 3. Clearly, some error occurs here due to the localization of the model's current to these discs.

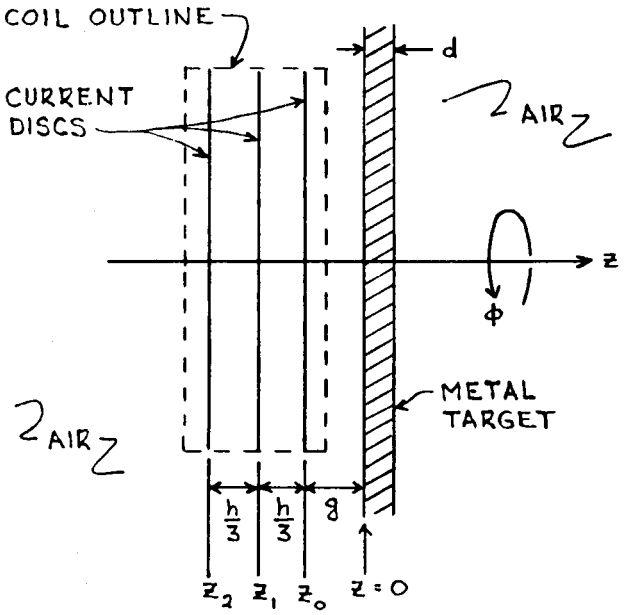

FIGURE 3
CURRENT DISC MODEL OF COIL

Figure 4 shows the Hankel space transmission line configuration corresponding to the three current sheet model of the coil next to the target. All of the Hankel space calculations are based upon this model.

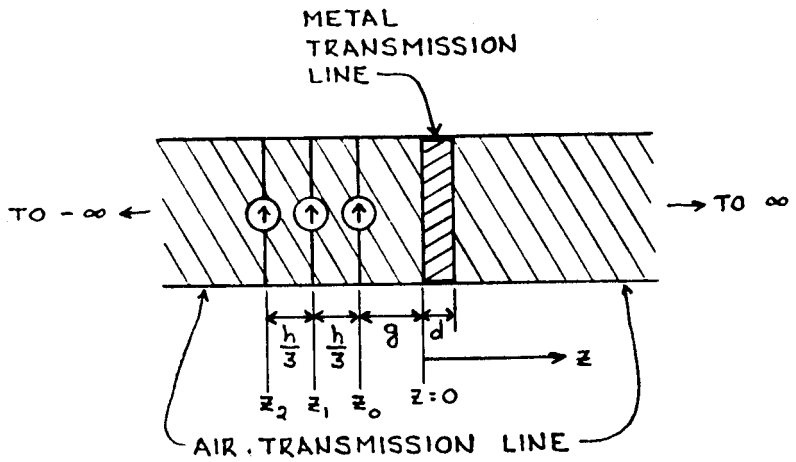

FIGURE 4
HANKEL SPACE TRANSMISSION LINE MODEL
OF COIL AND TARGET

CHAPTER FOUR

ANALYSIS SIRUCTURE

4.1 INTRODUCTION

In this chapter, the transmission line model of the coil and target developed in Chapter 3 and shown in Figure 4 is examined mathematically using conventional transmission line theory to predict the Fourier-Hankel space behavior of the model when it is in the sinusoidal steady state. The analyses performed in this chapter will assume each of the three current sources in Figure 4 has unit phasor value. In view of the analogy developed in Chapter 3, use will be made of the terms current and voltage in connection with the transmission line model to stand for the Fourier-Hankel transforms of the radial magnetic induction $B_r(z,r,t)$ and the azimuthal electric intensity $E_\phi(z,r,t)$ respectively. Throughout this chapter, reference should be made to Figure 4 for insight into the equations written.

4.2 METHOD OF CALCULATING COIL IMPEDANCE

Although the part of the coil impedance that is independent of the properties of the ribbon conductor used to wind the coil is calculated in Hankel space, as shown in this section, one must begin the derivation of the expresion for the impedance in Fourier space. Only in the frequency domain does the concept of impedance make sense. The coil impedance will be calculated at a frequency omega by exciting the coil with a current source of phasor value 1, and finding the phasor voltage response at the coil terminals. The coil impedance is then numerically equal to this

voltage response.

The real (Fourier) space model of the coil is three ideal discs of azimuthally directed uniform surface current. The electric fields induced in the different parts of this model need to be related to the voltage that exists between the coil terminals. To do this, the voltage appearing at the coil terminals will be approximated by the arithmetic average of the voltages induced at the locations of the three discs of the model. Symbolically,

$$Z = \frac{\tilde{V}}{\tilde{I}} = \frac{\tilde{V}}{1} = \tilde{V} = \frac{1}{3}\left(\tilde{V}_0 + \tilde{V}_1 + \tilde{V}_2\right)$$

where $\tilde{V}_k$ represents the voltage induced at the location of the disc with axial coordinate z_k.

Because of the symmetry of the model, the voltage induced on a circular path (centered on the z axis) of radius r and axial coordinate z_k will be given by

$$2\pi r\, E_\phi(z_k, r, \omega)$$

The average voltage induced on the infinite number of circular paths between $r=R_1$ and $r=R_2$ is

$$\frac{1}{R_2 - R_1} \int_{R_1}^{R_2} 2\pi r\, E_\phi(z_k, r, \omega)\, dr$$

Multiplication of this expression by N, the number of turns in the actual coil, yields

$$\tilde{V}_k = \frac{2\pi N}{R_2 - R_1} \int_{R_1}^{R_2} r\, E_\phi(z_k, r, \omega)\, dr$$

which is the model-predicted voltage induced on an infinitesimally thin N turn coil having an inner radius R_1 and an outer radius R_2 located at z_k.

Averaging these induced voltages over the three discs results in the phasor coil voltage

$$\tilde{V} = \frac{1}{3}\left\{ \frac{2\pi N}{R_2 - R_1} \int_{R_1}^{R_2} r \sum_{i=0}^{2} E_\phi(z_i, r, \omega)\, dr \right\} \tag{15}$$

$$\tilde{V} = Z$$

Because this expression is numerically equal to the coil impedance, the symbol $\tilde{V}$ will be replaced by the symbol Z in further appearances of this expression. The E fields that appear in (15) are frequency domain (Fourier space) E fields. In terms of the Fourier–Hankel space E fields, these Fourier space E fields can be written as

$$E_\phi(z_k, r, \omega) = \int_0^\infty E_\phi(z_k, \lambda, \omega)\, \lambda\, J_1(\lambda r)\, d\lambda \tag{16}$$

where again the list of arguments is used to distinguish between different functions. Specifically, $E_\phi(z_k,r,\omega)$ is the Fourier transform of the real space azimuthal electric intensity $E_\phi(z_k,r,t)$, and $E_\phi(z_k, \lambda, \omega)$ is the Fourier–Hankel transform of the real space azimuthal electric intensity $E_\phi(z_k,r,t)$. Substituting (16) into (15) yields

$$Z = \frac{1}{3}\frac{2\pi N}{R_2 - R_1} \int_{R_1}^{R_2} \left[\sum_{i=0}^{2} \int_0^\infty E_\phi(z_i, \lambda, \omega)\, \lambda\, J_1(\lambda r)\, d\lambda \right] r\, dr$$

Interchanging the order of integration,

$$Z = 2\pi \int_0^\infty \left[\frac{N}{3(R_2 - R_1)} \int_{R_1}^{R_2} J_1(\lambda r)\, r\, dr \right] \sum_{i=0}^{2} E_\phi(z_i, \lambda, \omega)\, \lambda\, d\lambda$$

$$Z = 2\pi \int_0^\infty K'(\lambda) \sum_{i=0}^{2} E_\phi(z_i, \lambda, \omega)\, \lambda\, d\lambda \tag{17}$$

where

$$K'(\lambda) = \frac{N}{3(R_2 - R_1)} \int_{R_1}^{R_2} J_1(\lambda r)\, r\, dr$$

is the Hankel transformed current corresponding to an infinitesimally thin N turn coil of inner radius R_1 and outer radius R_2, carrying a phasor current of strength 1/3.

Expression (17) contains three Fourier-Hankel space electric fields (transmission line voltages) that conceptually arose from Fourier space phasor currents of value 1/3 on each of the three discs in Figure 3. The "scaling factor" that relates Fourier-Hankel space fields due to unity Fourier space phasor coil current to Fourier-Hankel space voltages and currents due to unity phasor current in each of the three current sources in Figure 4 is $K'(\lambda)$. Then in terms of the Fourier-Hankel space voltage $E'_\phi(z_k, \lambda, \omega)$ due to unity phasor current in each of the Figure 4 current sources, (17) becomes

$$Z = 2\pi \int_0^\infty [K'(\lambda)]^2 \sum_{i=0}^{2} E'_\phi(z_i, \lambda, \omega)\, \lambda\, d\lambda \qquad (18)$$

Expression (18) is the result that will be used to calculate the terminal impedance of the coil.

4.3 RADIAL MAGNETIC INDUCTION AND AZIMUTHAL ELECTRIC INTENSITY

4.3.1 Target Surface Facing Coil

Using the results derived in Chapter 3, the characteristic impedance and the complex propagation constant of the air transmission line and the metal transmission line, referred to hereafter as the air line and the metal line respectively, will be calculated. For the air line, the conductivity sigma is equal to zero, and so

$$\mathcal{Z}_a = \frac{-j\omega\mu}{\sqrt{\lambda^2 + j\omega\mu\sigma}} = \frac{-j\omega\mu}{\lambda}$$

$$\gamma_a = \sqrt{\lambda^2 + j\omega\mu\sigma} = \lambda$$

For the metal line, no simplification is possible and so

$$\mathcal{Z}_m = \frac{-j\omega\mu}{\sqrt{\lambda^2 + j\omega\mu\sigma}}$$

$$\gamma_m = \sqrt{\lambda^2 + j\omega\mu\sigma}$$

According to the analogy developed in Chapter 3, calculation of the total current and voltage at z=0 in Figure 4 is equivalent to calculation of the radial magnetic induction B_r and the azimuthal electric intensity E_o on the coil side face of the target. This current and voltage calculation is performed by replacing the transmission line configuration for all z>0 with its equivalent input impedance. Note that both sides of the metal line are connected to infinite lengths of air transmission line with characteristic impedance Z_a. The equivalent impedance looking to the right at z=0 in Figure 4 is

$$\mathcal{Z}(0) = \mathcal{Z}_m \frac{\mathcal{Z}_a + \mathcal{Z}_m \tanh(\gamma_m d)}{\mathcal{Z}_m + \mathcal{Z}_a \tanh(\gamma_m d)} \tag{19}$$

Using this equivalent impedance, the current reflection coefficient at z=0 as seen from the air line is

$$\rho_H = \frac{\mathcal{Z}_a - \mathcal{Z}(0)}{\mathcal{Z}_a + \mathcal{Z}(0)}$$

and the total current at z=0 is then

$$\hat{I}_{total} = \hat{I}_{inc} + \hat{I}_{refl} = (1 + \rho_H)\,\hat{I}_{inc} \tag{20}$$

in terms of the incident current $\hat{I}_{inc}$, which must be due solely to the three current sources. Expression (20) may be simplified as follows.

$$\hat{I}_{total} = \left(1 + \frac{Z_a - Z(0)}{Z_a + Z(0)}\right) \hat{I}_{inc} = \frac{2Z_a}{Z_a + Z(0)} \hat{I}_{inc} \qquad (21)$$

Substituting (19) into (21) yields

$$\hat{I}_{total} = 2\hat{I}_{inc} \frac{Z_a}{Z_a + Z_m \dfrac{Z_a + Z_m \tanh(\gamma_m d)}{Z_m + Z_a \tanh(\gamma_m d)}}$$

which, upon replacing Z_a and Z_m by their defining expressions gives

$$\hat{I}_{total} = 2\hat{I}_{inc} \frac{1}{1 + \dfrac{\lambda}{\sqrt{\lambda^2 + j\omega\mu\sigma}} \dfrac{1 + \dfrac{\lambda}{\sqrt{\lambda^2 + j\omega\mu\sigma}} \tanh(\gamma_m d)}{\dfrac{\lambda}{\sqrt{\lambda^2 + j\omega\mu\sigma}} + \tanh(\gamma_m d)}} \qquad (22)$$

Now consider the current source in Figure 4 closest to the target. This source produces an incident current on the metal line at z=0 given by

$$\hat{I}_{inc\,o} = \frac{1}{2} e^{-\gamma_a g} = \frac{1}{2} e^{-\lambda g}$$

where the factor 1/2 comes from the equal division of the unity phasor amplitude current to both sides of the air line containing the current source. Total current incident at z=0 is by superposition given by

$$\hat{I}_{inc} = \frac{1}{2} e^{-\lambda g} + \frac{1}{2} e^{-\lambda\left(g + \frac{h}{3}\right)} + \frac{1}{2} e^{-\lambda\left(g + \frac{2h}{3}\right)}$$

$$\hat{I}_{inc} = \frac{1}{2} e^{-\lambda g}\left(1 + e^{-\frac{\lambda h}{3}} + e^{-\frac{2\lambda h}{3}}\right) \qquad (23)$$

Substituting (23) into (22) yields

$$\hat{I}_{total} = \frac{e^{-\lambda g}\left(1 + e^{-\frac{\lambda h}{3}} + e^{-\frac{2\lambda h}{3}}\right)}{1 + \frac{\lambda}{\sqrt{\lambda^2 + j\omega\mu\sigma}} \frac{1 + \frac{\lambda}{\sqrt{\lambda^2 + j\omega\mu\sigma}} \tanh(\gamma_m d)}{\frac{\lambda}{\sqrt{\lambda^2 + j\omega\mu\sigma}} + \tanh(\gamma_m d)}} \qquad (24)$$

for the total steady state current I_{total} at z=0 due to unit strength complex sinusoidal excitation in each of the three current sources. Multiplying (24) by $K'(\lambda)I(\omega)$, where $I(\omega)$ is the Fourier transform of the current in the coil (and multiplication by $K'(\lambda)$ transforms a unity Fourier space current into the corresponding Fourier-Hankel space current), yields the desired result

$$\hat{I}_{(z=0)} = \frac{I(\omega)\, K'(\lambda)\, e^{-\lambda g}\left(1 + e^{-\frac{\lambda h}{3}} + e^{-\frac{2\lambda h}{3}}\right)}{1 + \frac{\lambda}{\sqrt{\lambda^2 + j\omega\mu\sigma}} \frac{1 + \frac{\lambda}{\sqrt{\lambda^2 + j\omega\mu\sigma}} \tanh(\gamma_m d)}{\frac{\lambda}{\sqrt{\lambda^2 + j\omega\mu\sigma}} + \tanh(\gamma_m d)}} \qquad (25)$$

for the Fourier-Hankel transform of the radial magnetic induction B_r on the coil side face of the metal target when the coil current spectrum is $I(\omega)$.

Calculation of the voltage is almost identical to the calculation of the current performed above. The voltage reflection coefficient ρ_E is the negative of the current reflection coefficient,

$$\rho_E = \frac{Z(0) - Z_a}{Z(0) + Z_a} .$$

Total voltage at z=0 is

$$\hat{V}_{total} = \hat{V}_{inc} + \hat{V}_{refl} = (1 + \rho_E)\,\hat{V}_{inc} \qquad (26)$$

in terms of the incident voltage $\hat{V}_{inc}$. Expression (26) may be simplified as

$$\hat{V}_{total} = \left(1 + \frac{Z(0) - Z_a}{Z(0) + Z_a}\right)\hat{V}_{inc} = \frac{2Z(0)}{Z_a + Z(0)} \qquad (27)$$

Substituting (19) into (27),

$$\hat{V}_{total} = 2\hat{V}_{inc}\,\frac{Z_m\,\dfrac{Z_a + Z_m \tanh(\gamma_m d)}{Z_m + Z_a \tanh(\gamma_m d)}}{Z_a + Z_m\,\dfrac{Z_a + Z_m \tanh(\gamma_m d)}{Z_m + Z_a \tanh(\gamma_m d)}}$$

which, upon replacing Z_a and Z_m by their defining expressions, gives

$$\hat{V}_{total} = \frac{2\hat{V}_{inc}}{1 + \dfrac{\sqrt{\lambda^2 + j\omega\mu\sigma}}{\lambda}\;\dfrac{\dfrac{\lambda}{\sqrt{\lambda^2 + j\omega\mu\sigma}} + \tanh(\gamma_m d)}{1 + \dfrac{\lambda}{\sqrt{\lambda^2 + j\omega\mu\sigma}}\tanh(\gamma_m d)}} \qquad (28)$$

Total incident voltage $\hat{V}_{inc}$ at z=0 is given by

$$\hat{V}_{inc} = Z_a \hat{I}_{inc} = \frac{j\omega\mu}{2\lambda}\, e^{-\lambda g}\left(1 + e^{-\frac{\lambda h}{3}} + e^{-\frac{2\lambda h}{3}}\right)$$

using (23) for $\hat{I}_{inc}$. Substituting this expression for $\hat{V}_{inc}$ into (28) yields

$$\hat{V}_{total} = \frac{\dfrac{j\omega\mu}{\lambda}\, e^{-\lambda g}\left(1 + e^{-\frac{\lambda h}{3}} + e^{-\frac{2\lambda h}{3}}\right)}{1 + \dfrac{\sqrt{\lambda^2 + j\omega\mu\sigma}}{\lambda}\;\dfrac{\dfrac{\lambda}{\sqrt{\lambda^2 + j\omega\mu\sigma}} + \tanh(\gamma_m d)}{1 + \dfrac{\lambda}{\sqrt{\lambda^2 + j\omega\mu\sigma}}\tanh(\gamma_m d)}} \qquad (29)$$

for the total voltage at z=0 due to unit strength complex sinusoidal excitation in each of the three current sources. Multiplying (29) by $K'(\lambda)I(\omega)$ yields the desired result

$$\hat{V}(z=0) = \frac{I(\omega)K'(\lambda)\frac{j\omega\mu}{\lambda}e^{-\lambda g}\left(1+e^{-\frac{\lambda h}{3}}+e^{-\frac{2\lambda h}{3}}\right)}{1+\frac{\sqrt{\lambda^2+j\omega\mu\sigma}}{\lambda}\;\frac{\frac{\sqrt{\lambda^2+j\omega\mu\sigma}}{\lambda}+\tanh(\gamma_m d)}{1+\frac{\sqrt{\lambda^2+j\omega\mu\sigma}}{\lambda}\tanh(\gamma_m d)}} \tag{30}$$

for the Fourier-Hankel transform of the azimuthal electric intensity E_ϕ on the coil side face of the target when the coil current spectrum is $I(\omega)$.

4.3.2 Target Surface Opposite Coil

Knowing the total voltage and current at z=0 (derived in Section 4.3.1 and given by (30) and (25) respectively) allows a simple transmission line inverse chain matrix calculation of the total voltage and current at z=d, which are the Fourier-Hankel transforms of the azimuthal electric intensity E_ϕ and the radial magnetic induction B_r on the surface of the metal target opposite the coil. Denoting these transforms of the fields on the coil side face of the target by $\hat{V}_n$ (given by (30) above) and $\hat{I}_n$ (given by (25) above),

$$\hat{V}_f = \hat{V}_n\cosh(\gamma_m d) - Z_m\hat{I}_n\sinh(\gamma_m d) \tag{31}$$

$$\hat{I}_f = -\hat{V}_n\frac{\sinh(\gamma_m d)}{Z_m} + \hat{I}_n\cosh(\gamma_m d) \tag{32}$$

where $\hat{V}_f$ and $\hat{I}_f$ denote total voltage (electric intensity) and current (magnetic induction) on the surface of the target opposite the coil.

4.4 CALCULATION OF THE AXIAL MAGNETIC FIELD USING THE TRANSMISSION LINE MODEL

The procedure used for calculating the force on the target is described in the next section, and requires both the radial and the axial components of the magnetic induction on the target surface next to the coil. The radial component of the magnetic intensity is available from the transmission line model by performing inverse Hankel and Fourier transformations on the calculated transmission line current at z=0, as discussed in Section 4.3.1. By using equation (2) in Chapter 3, it is also possible to calculate the axial component of the magnetic intensity (which does not have a transmission line analog) from the transmission line voltage. This will now be shown.

The azimuthal electric field is given in Fourier space by

$$E_\phi(z,r,\omega) = \mathcal{H}^{-1}\{V(z,\lambda,\omega)\} = \int_0^\infty V(z,\lambda,\omega)\,\lambda\,J_1(\lambda r)\,d\lambda \qquad (33)$$

Substituting (33) into equation (2),

$$H_z(z,r,\omega) \quad \frac{-1}{j\omega\mu}\frac{1}{r}\frac{\partial}{\partial r}\{r\,E_\phi(z,r,\omega)\}$$

$$H_z(z,r,\omega) = \frac{-1}{j\omega\mu r}\frac{\partial}{\partial r}\left\{r\int_0^\infty V(z,\lambda,\omega)\,\lambda\,J_1(\lambda r)\,d\lambda\right\} \qquad (34)$$

Interchanging the order of partial differentiation and integration in (34),

$$H_z(z,r,\omega) = \frac{-1}{j\omega\mu r}\int_0^\infty \frac{\partial}{\partial r}\{\lambda r\,J_1(\lambda r)\}\,V(z,\lambda,\omega)\,d\lambda \qquad (35)$$

Using the identity

$$\frac{d}{dx}\left\{ x\, J_1(x) \right\} = x\, J_0(x)$$

(35) becomes

$$H_z(z, r, \omega) = \frac{-1}{j\omega\mu} \int_0^\infty V(z, \lambda, \omega)\, \lambda^2\, J_0(\lambda r)\, d\lambda \qquad (36)$$

Equation (36) states that the axial component of the magnetic intensity H_Z in Fourier space is given by the zero order inverse Hankel transform of the transmission line voltage at the corresponding z coordinate multiplied by lambda, with the result divided by $j\omega\mu$. Inverse Fourier transformation of the right hand side of (36) yields the desired time domain axial magnetic intensity.

4.5 FORCE BETWEEN TARGET AND COIL

The procedure for calculating the total force between the target and the coil utilizes the Maxwell stress tensor, and is performed in real space (using the time domain fields). Stratton [41] shows that the total force F transmitted by a time varying electromagnetic field across a closed surface S is given by

$$\bar{F} = \oint_S \left[\varepsilon(\bar{E}\circ\hat{n})\bar{E} + \frac{1}{\mu}(\bar{B}\circ\hat{n})\bar{B} - \frac{1}{2}\left(\varepsilon E^2 + \frac{B^2}{\mu}\right)\hat{n} \right] da$$

where n is a unit vector normal to the surface. The closed surface is taken to be the plane z=0 (the coil side face of the target, "closed" at infinity). Since $\hat{n}=\hat{z}$, this integral reduces to

$$\bar{F} = \int_{r=0}^{\infty} \int_{\phi=0}^{2\pi} \left[\frac{B_z}{\mu}(B_z\hat{z} + B_r\hat{r}) - \frac{1}{2}\left(\varepsilon E_\phi^2 + \frac{B_z^2 + B_r^2}{\mu}\right)\hat{z} \right] r\, d\phi\, dr$$

The total force tending to separate coil and target is just the z component of this force,

$$F_z = 2\pi \int_{r=0}^{\infty} \left(\frac{B_z^2}{2\mu} - \frac{\varepsilon E_\phi^2}{2} - \frac{B_r^2}{2\mu} \right) r \, dr$$

$$F_z = \frac{\pi}{\mu} \int_0^{\infty} (B_z^2 - B_r^2) \, r \, dr - \pi\varepsilon \int_0^{\infty} E_\phi^2 \, r \, dr \qquad (37)$$

Calculations of the fields E_ϕ, B_r, and B_z in the prototype experimental EIDI configuration described in Chapter 5 showed that the second integral in (37) is insignificant compared to the first integral. Some feeling for why this is true can be obtained by comparing the constants that multiply each of the integrals in (37).

$$\frac{\pi}{\mu} = \frac{\pi}{4\pi \times 10^{-7}} = 2.5 \times 10^{6}$$

$$\pi\varepsilon \doteq \frac{\pi \, 10^{-9}}{36\pi} \doteq 2.8 \times 10^{-11}$$

Accordingly, (37) may be approximated by

$$F_z(t) = \frac{\pi}{\mu} \int_0^{\infty} [B_z^2(t) - B_r^2(t)] \, r \, dr \qquad (38)$$

Equation (38) is the result used to calculate total force versus time.

4.6 IMPULSE DELIVERED TO TARGET

The impulse delivered to the stationary target is by definition given by the integral

$$I = \int_0^{\infty} F_z(t) \, dt \qquad (39)$$

where $F_Z(t)$ is calculated using (38).

CHAPTER FIVE

A SPECIFIC SYSTEM EXAMPLE, INCLUDING EXPERIMENTAL RESULTS

5.1 DEFINITION OF THE SYSTEM

The prototype EIDI system constructed at The Wichita State University, and the results of the tests made on that system, have been described in detail by Dr. Robert Schrag [3]. Most of the material in this Chapter has been excerpted from Dr. Schrag's paper.

Figure 5 shows the prototype EIDI energy discharge system, omitting the capacitor charging circuit and the thyristor firing circuit. Two identical pulsing coils were operated in series, because that was the arrangement used in most of the de-icing tests. However, only one of the two coils was utilized in the coil-target assembly, which is detailed in Figure 6.

The effective gap between the coil (copper) surface and the near surface of the target was .078". A .032" thick 2024 T3 Aluminum disc was used as the target. Diameter of this disc was 5 inches. Two .05" thick phenolic spacer plates were used, one to maintain a fixed distance between the coil and the target, and the other to maintain the distance between the target and the rigid wooden support that prevented motion of the target. These plates could be removed, and a special magnetic field measuring plate (described in Section 5.4) inserted in their place in order to make measurements of the magnetic induction close to the surface of the target. Each coil consisted of 30 turns of .024" X .188" rectangular copper wire spirally wound in a single layer from an inner radius of .125" to an outer radius of 1". The initial capacitor voltage

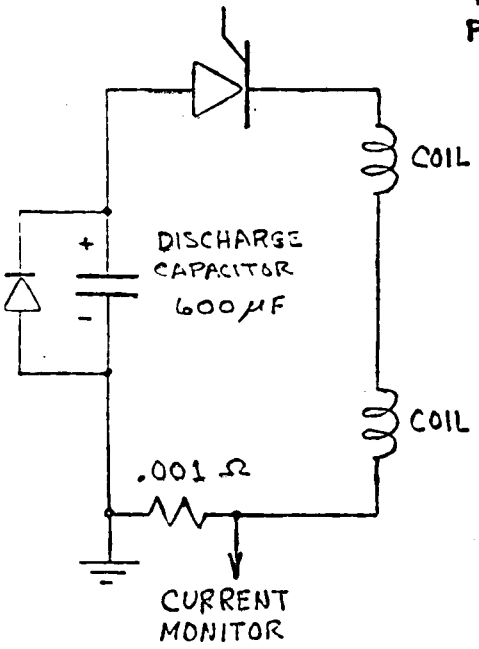

FIGURE 5
ENERGY DISCHARGE CIRCUIT

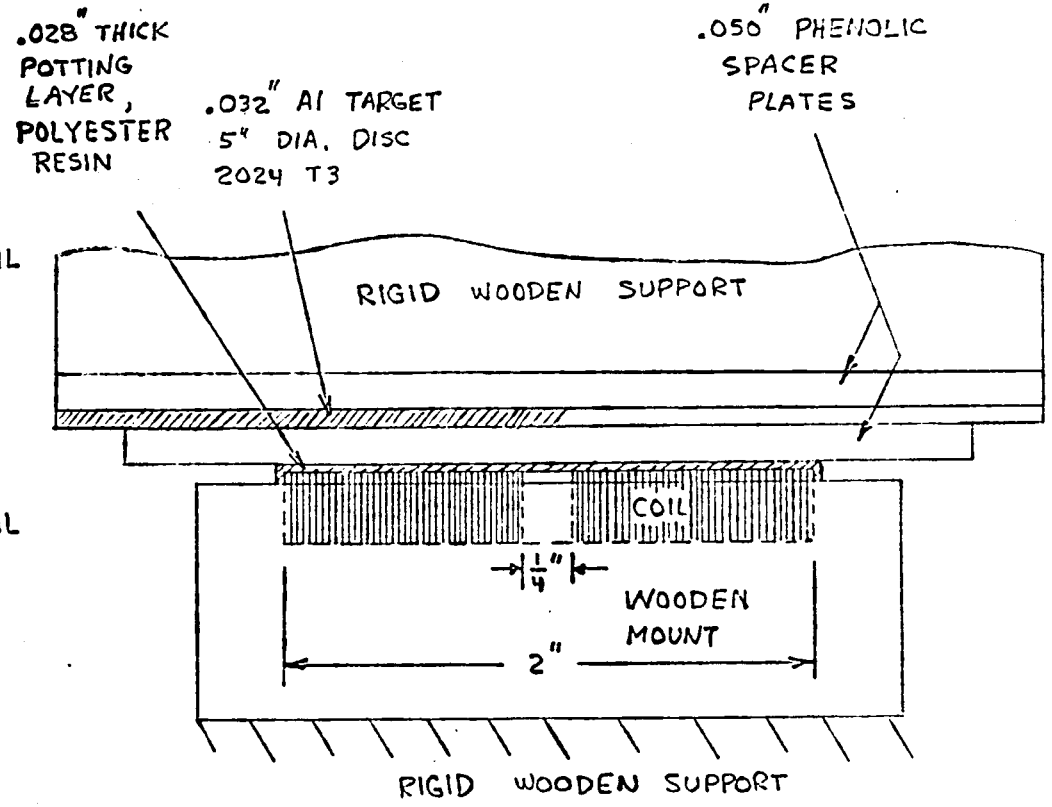

FIGURE 6
DETAILS OF COIL-TARGET
ASSEMBLY

COIL DATA:
30 TURNS OF .024" × .188"
RECTANGULAR COPPER
WIRE, SINGLE LAYER
SPIRALLY WOUND

utilized for the experimental study was 400 volts.

5.2 COIL IMPEDANCE MEASUREMENTS

Impedance measurements on the coil next to the target were made using an impedance bridge. The inductance determined by these measurements, for several frequencies, appears in the table below. Impedance measurements were also made on the coil when the metal target was removed. The real part of the impedance measured on the coil without the target in place was subtracted from the real part of the impedance measured on the coil with the target in place. This increase in resistance due to the target is given in the table below.

RESISTANCE INCREASE AND INDUCTANCE - COIL AND METAL TARGET

Frequency (Hertz)	Inductance (Microhenries)	Resistance Increase (Milliohms)
500	18.6	8.2
1000	17.0	23.0
2000	14.6	48.0
4000	12.6	77.0

5.3 CURRENT WAVEFORM

Initially, current in the coil was measured indirectly by measuring the voltage across the .001 ohm non-inductive resistor in Figure 5. Difficulties with this approach prompted the purchase of a current transformer from Pearson Electronics, Inc. Using this transformer and a storage oscilloscope, the current shown in Figure 7 was observed.

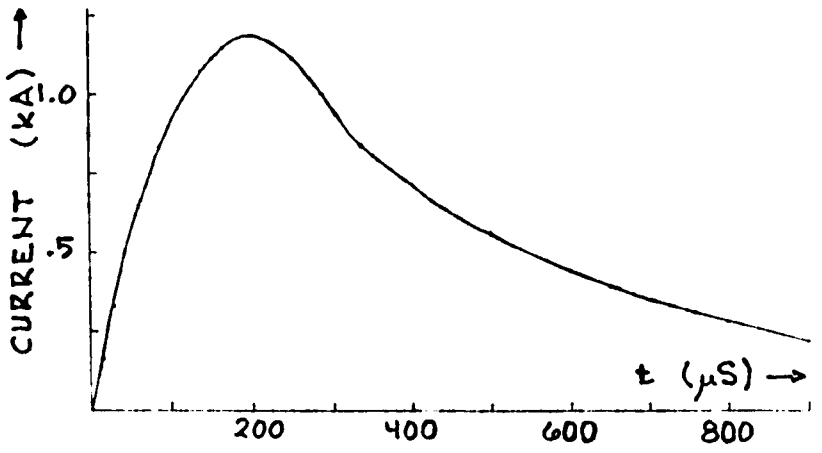

FIGURE 7
COIL CURRENT

5.4 MAGNETIC FIELD MEASUREMENTS

A magnetic field measuring plate was constructed in the manner illustrated in Figure 8. Shallow concentric grooves were cut into both sides of a .05" phenolic disc, with radius increments of .2", starting

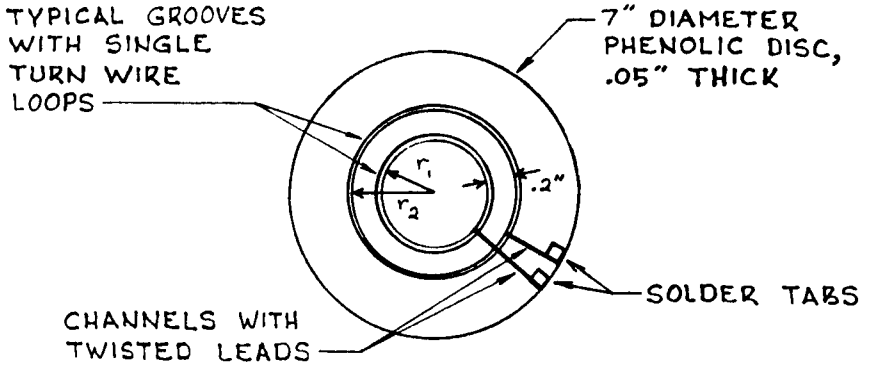

FIGURE 8
PARTIAL ILLUSTRATION
FIELD MEASURING PLATE

at r=.2" and ending at r=2.0". Single turn loops of .006" diameter wire

were then cemented into these grooves, and their twisted leads brought out to solder tabs through radial channels.

For measuring the fields on either side of the target, the measuring plate simply substituted for the corresponding phenolic spacer plate in Figure 6. A measurement of the axial flux density was derived from the induced voltage in any two neighboring loops connected in series opposition. For the two loops illustrated in Figure 8, for example,

$$B_z(t) = 1550 \frac{\int_0^t v(\tau)\, d\tau}{\pi(r_2^2 - r_1^2)}$$

where B_Z is in teslas, r is in inches, and v is in volts. This value is the average axial flux density over the area between the two induction loops. In the further use of this result, this flux density will be assumed to apply at a radius midway between the two loops.

To measure the radial component of flux density at any radius, the front and back loops at that radius are connected in series opposition, and calculations are made from

$$B_r(t) = 1550 \frac{\int_0^t v(\tau)\, d\tau}{2\pi r h}$$

where r is the radius of the two induction loops and h is their separation, both in inches.

Plots of the magnetic induction fields obtained from these tests with the target in place are shown at selected radii in Figures 9, 10, 11, and 12. All B_r data showed an anomolous behavior (irregularities) at r=.4" relative to r=.6". A separate check was made, in which the plate was reversed (interchanging the two sides). This produced a reversal of the irregularities, so the effect was probably due to an

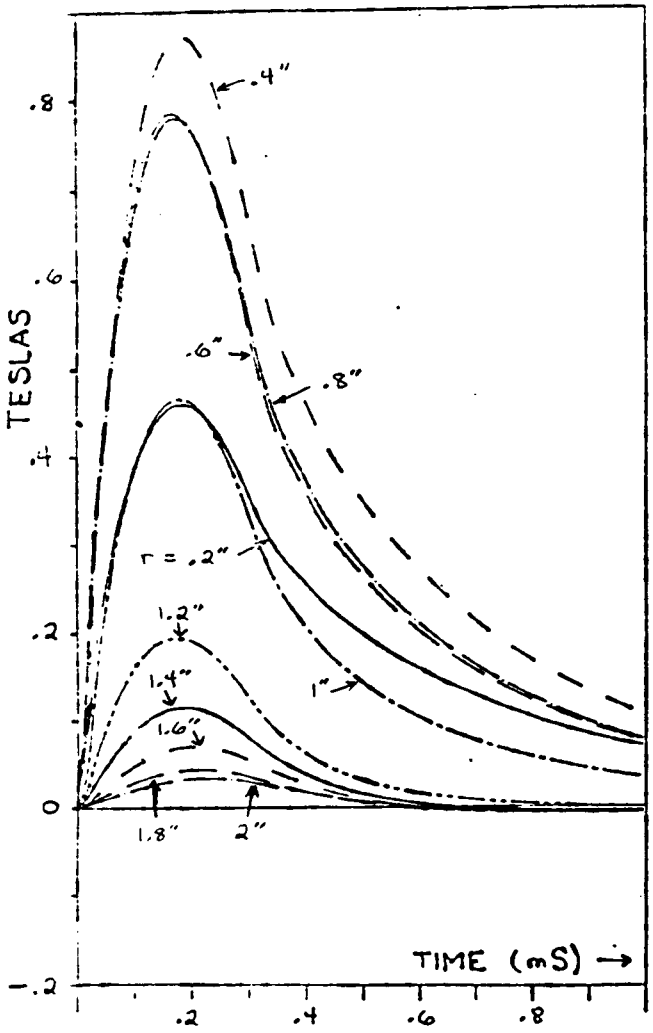

FIGURE 9
MEASURED B_r VERSUS TIME
NEAR SIDE OF TARGET

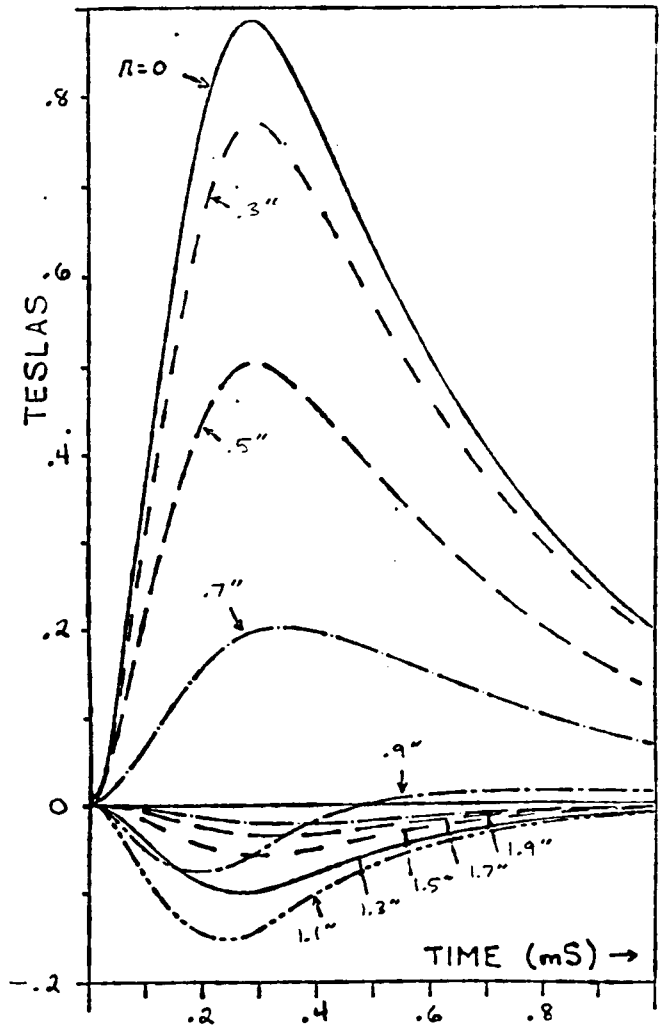

FIGURE 10
MEASURED B_z VERSUS TIME
NEAR SIDE OF TARGET

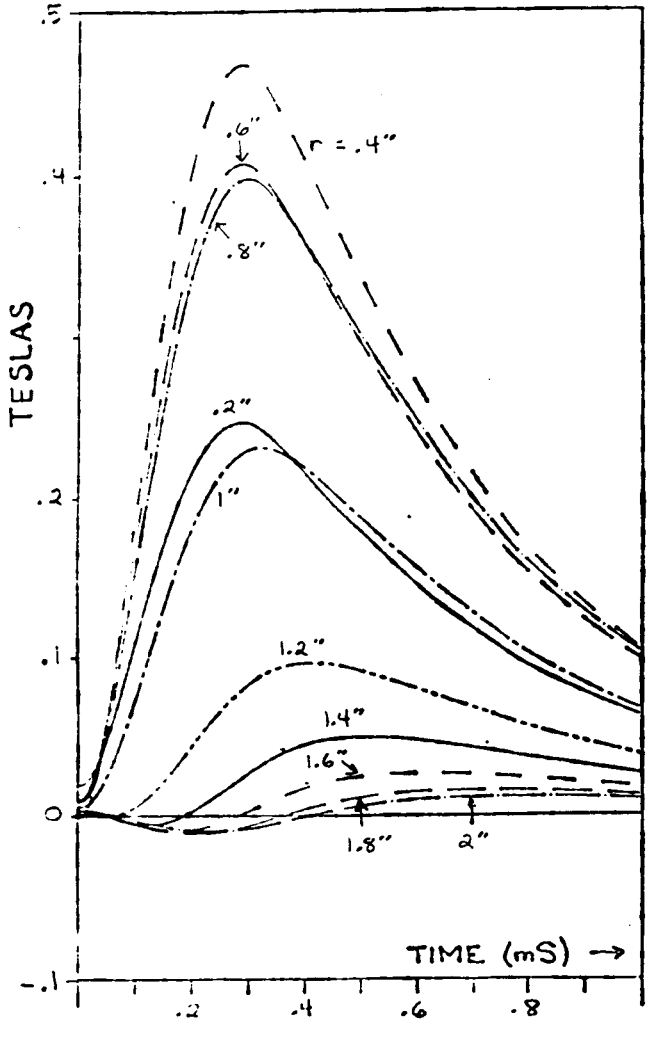

FIGURE 11
MEASURED B_r VERSUS TIME
FAR SIDE OF TARGET

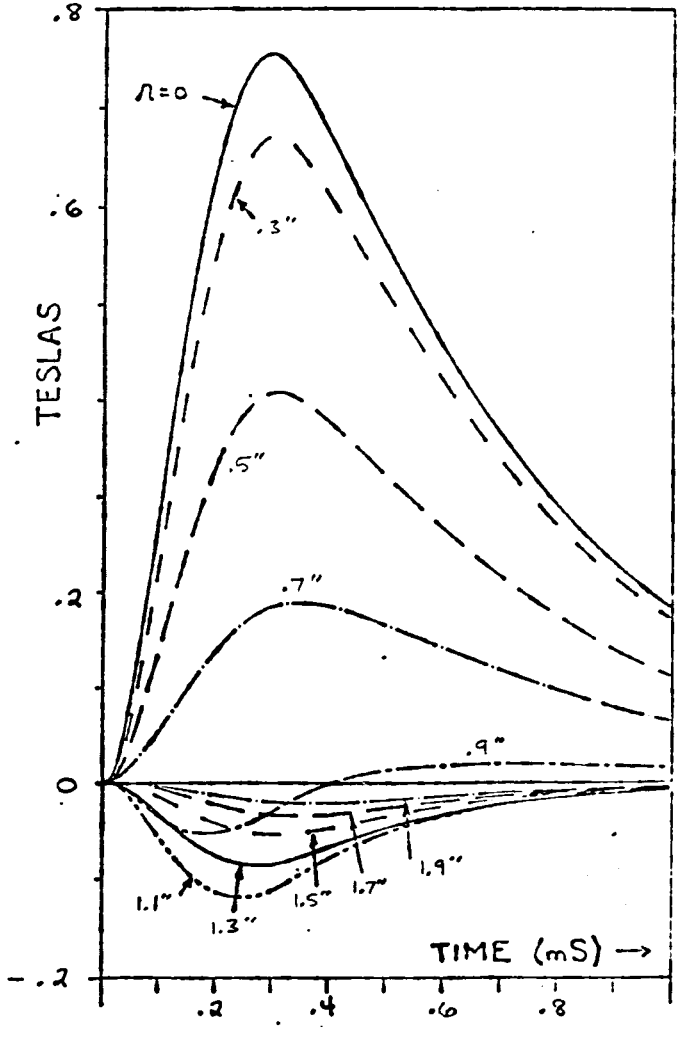

FIGURE 12
MEASURED B_z VERSUS TIME
FAR SIDE OF TARGET

inaccuracy in the construction of the plate.

5.5 MEASUREMENT OF IMPULSE TO TARGET

The final step in the experiment was the measurement of the impulse delivered to the target when the capacitor was discharged through the coil. This was done indirectly, using a ballistic pendulum. The impulse so measured was approximately .012 lb-sec.

CHAPTER SIX

COMPUTER ANALYSIS ON THE SYSTEM EXAMPLE

6.1 INTRODUCTION

Theoretical background for the numerical computations described in this chapter were developed in Chapters 3 and 4. This chapter will concentrate on a description of the numerical methods used to implement the theoretical development contained in those earlier chapters to predict the performance of the prototype EIDI system described in Chapter 5. The sections that follow are arranged in the order of the Figure 1 Analysis Flow Diagram, beginning with Block 4 of that diagram. This is the order in which the computations were actually accomplished.

All computations were performed in FORTRAN 66 on an IBM 370. Source code was compiled with the IBM furnished G level compiler.

6.2 COIL IMPEDANCE

Equation (18) of Chapter 4, repeated below as equation (40), is the coil impedance predicted by the transmission line model. Numerical evaluation of the integral in (40) is discussed in this section.

$$Z(\omega) = 2\pi \int_0^\infty [K'(\lambda)]^2 \sum_{i=0}^{2} E'_\phi(z_i, \lambda, \omega)\, d\lambda \qquad (40)$$

Two common methods are in use to accomplish quadrature of an improper integral such as the integral above [21]. In the first method, a transformation of variables is performed prior to construction of an algorithm for estimating the value of the integral. This transformation is chosen in such a manner that the new integral has finite limits. The

second method simply replaces the infinite upper limit with a finite upper limit, selected such that the part of the integral thus ignored contributes little to the true value of the integral. This method can be employed only if the integrand decays sufficiently rapidly as the variable of integration increases. Since the controlling factor in the leading behavior of the asymptotic expansion, as lambda tends to infinity, of the integrand in (40) is $e^{-\lambda g}$, with g a constant, the second method was chosen for use in the numerical evaluation of (40).

A large amount of high quality mathematical software is available today [22], [23]. Because of the complexity and cost of writing quality mathematical algorithms, most numerical analysts suggest that complex scientific calculations be performed using algorithms written by experts [24], [25]. An 8 panel adaptive Newton-Cotes algorithm entitled QUANC8, described in [25], was chosen to perform the quadrature in (40). A user of QUANC8 may select the relative and absolute error performances desired, and the program then attempts to estimate the value of the integral within the selected error criteria. One of the parameters in the subroutine QUANC8 is an output variable that contains an estimated error bound on the returned value.

Direct computer evaluation of (40) consumes a large amount of CPU time, and is consequently expensive. This is due mostly to the appearance of the factor $[K'(\lambda)]^2$ in the integrand. (Note that $K'(\lambda)$ is defined by an integral containing a Bessel function. This makes K' oscillatory, shown in Figure 13.) It was possible to decrease this cost considerably by calculating $K'(\lambda)$ using QUANC8 and fitting a cubic spline function to the calculated $K'(\lambda)$ for use in evaluating (40). The algorithms used for generating the spline function coefficients and for

evaluating the spline function at a given argument are entitled SPLINE and SEVAL, respectively, and are described in [25].

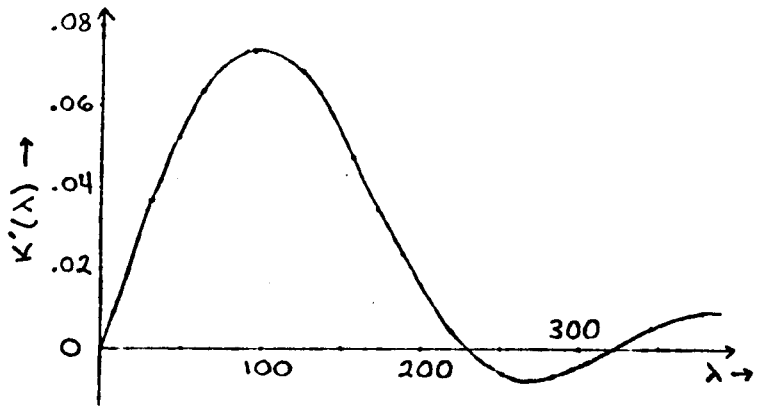

FIGURE 13
OSCILLATORY
NATURE OF $K'(\lambda)$

Once a spline function approximation for $K'(\lambda)$ was available, QUANC8 was used to individually estimate the real part (the coil resistance increase due to the metal target) and the imaginary part (the coil reactance) of (40) at selected frequencies. Initial estimates of the real and imaginary parts of the integral in (40) were obtained using an upper limit of 680. Following this, the programs were run again with an upper limit of 240. Little difference was seen in the results of the two calculations, leading to the conclusion that the coil resistance and inductance estimates were good. Figure 14 shows the effects of the upper limit of integration in evaluating the imaginary part of the integral in (40) for three different frequencies.

Figures 15 and 16 show the resistance increase and inductance calculated as described above. Measured values of these parameters are also shown for comparison.

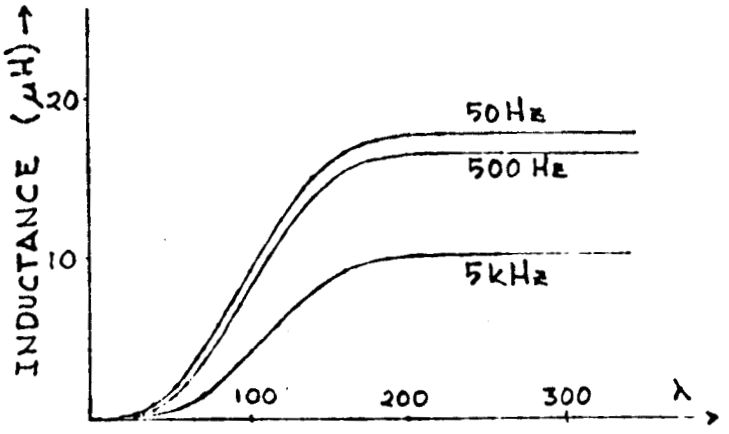

FIGURE 14
CALCULATED INDUCTANCE
VS.
UPPER INTEGRATION LIMIT

6.3 CURRENT WAVEFORM

6.3.1 Introduction

As discussed in Chapter 2, three factors preclude a simple calculation of the coil current in the EIDI prototype system. These three factors are the nonlinear diode and SCR, and the presence of the metal target next to the coil.

The effects of the target on the coil were taken into account by calculating the coil resistance increase and inductance at several frequencies, as described in the previous section. These two frequency dependent parameters were then approximated with cubic spline functions, again using the subroutine SPLINE. This provided the ability to calculate computationally inexpensive yet sufficiently accurate coil impedances for use in frequency domain circuit calculations.

6.3.2 Current Before Clamp Diode Conduction

Although the circuit is nonlinear due to the diode and SCR, it is

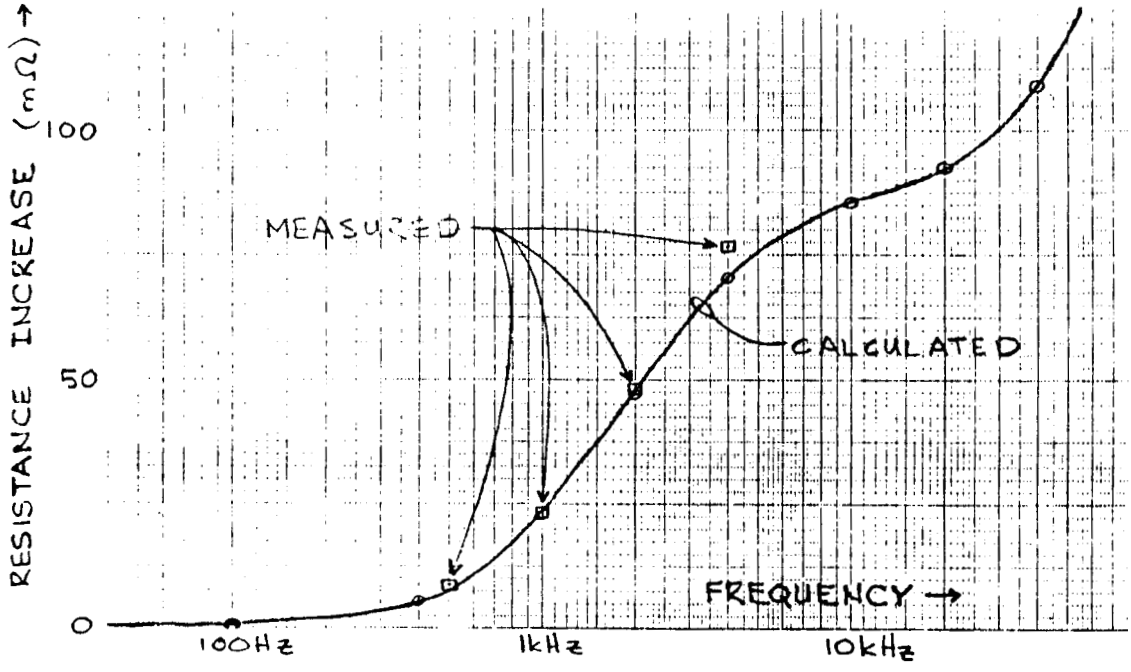

FIGURE 15
COIL RESISTANCE INCREASE DUE TO METAL TARGET

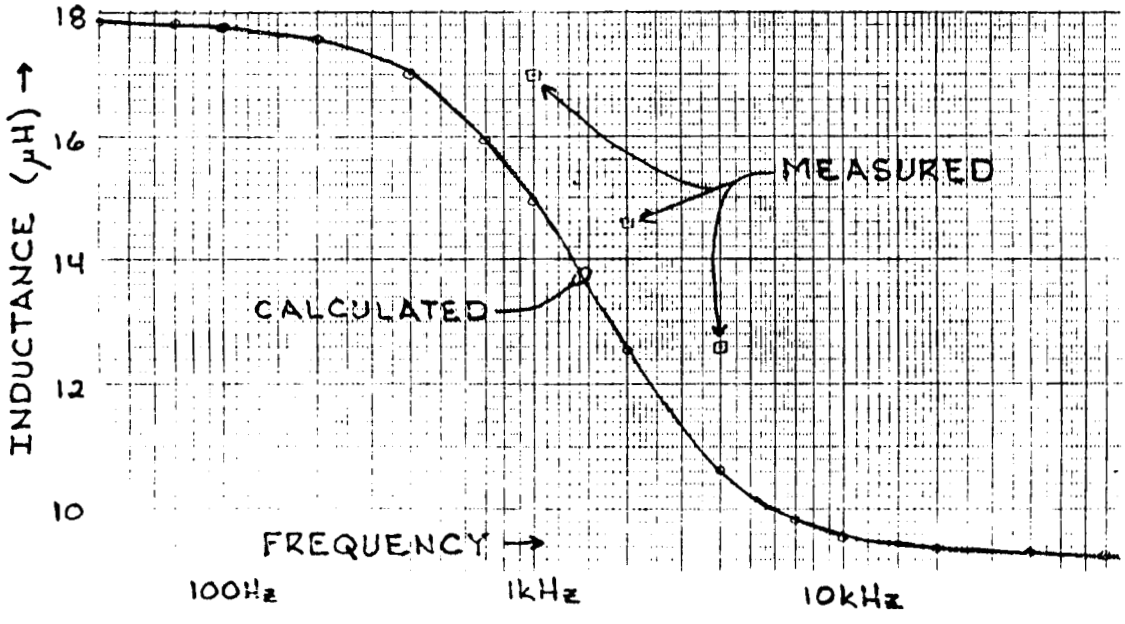

FIGURE 16
COIL INDUCTANCE IN PRESENCE OF METAL TARGET

amenable to treatment in a piecewise linear fashion. The frequency domain model of the circuit, valid between the time the SCR is initially triggered and the time the capacitor voltage becomes zero, is shown in Figure 17. In this Figure, the EIDI system capacitor is modeled as an ideal discharged capacitor in series with a voltage source. This voltage

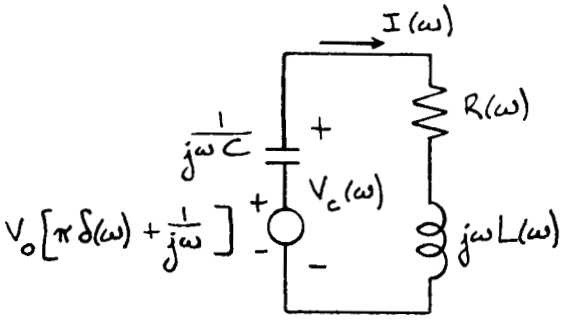

FIGURE 17
FREQUENCY DOMAIN CIRCUIT MODEL CLAMP DIODE OFF

source has a value of zero volts for all time prior to t=0. At t=0, it instantly rises to the amplitude and polarity V_o of the initial voltage on the actual capacitor, modeling the triggering of the SCR into instantaneous full forward conduction. Voltages and currents calculated from this model are good approximations to their corresponding quantities in the physical EIDI prototype circuit as long as the diode in parallel with the capacitor is not conducting.

The frequency dependent resistor appearing in Figure 17 is a composite lumped model of several energy loss mechanisms in the physical circuit. It includes the loss in the coil due to the presence of the metal target next to the coil (calculated as described in the previous section), resistance of the ribbon conductor used to wind the coil (corrected for skin effect), and the resistance of the cable used to connect the coil and capacitor. Resistance in the cable was modeled as frequency independent, with a measured D.C. value of .054 ohms. Coil winding

resistance was calculated from

$$R_{AC} = R_{DC} \; \text{Real}\left\{ \frac{h}{2} \frac{1+j}{\delta} \coth\left(\frac{h}{2} \frac{1+j}{\delta}\right)\right\}$$

where

R_{DC} = D.C. coil resistance = .0235 ohms
h = coil thickness = .00477 meters
δ = copper skin depth = $1/\sqrt{\pi f \mu \sigma}$
f = frequency in Hertz
μ = copper permeability = $4\pi \times 10^{-7}$ henries/meter
σ = copper conductivity = 3.48×10^{7} mhos/meter

Resistance R_{AC} is present in both the coil next to the target and the idler coil (see Figure 5).

Similarly, the frequency dependent inductance L in Figure 17 arises from more than one source. First, there is the inductance of the coil next to the target (calculated in the section above). Second, the idler coil and cable connecting the capacitor to the coil had a combined measured inductance of 23 microhenries, which was assumed to be independent of frequency. As these two inductances are in series in the circuit with negligible mutual inductance, they are added to obtain a value for L.

The leakage reactance and measuring circuit impedance reflected into the actual circuit by the current transformer used to measure the current were felt to be too small to be significant, and were not included in the Figure 17 model.

By inspection, the Fourier transform of the current in Figure 17 is given by

$$I(\omega) = \frac{V_o\left[\pi \delta(\omega) + \frac{1}{j\omega}\right]}{\frac{1}{j\omega C} + R(\omega) + j\omega L(\omega)}$$

$$I(\omega) = \frac{CV_o\left[\pi j\omega \delta(\omega) + 1\right]}{1 + j\omega C R(\omega) - \omega^2 C L(\omega)}$$

$$I(\omega) = \frac{CV_o}{1 - \omega^2 CL(\omega) + j\omega CR(\omega)} \tag{41}$$

Note that the delta distribution multiplies its own argument, and consequently contributes nothing to the time domain current i(t). Equation (41) is the basis for the current calculation, valid until the capacitor voltage becomes zero and the clamp diode in parallel with the capacitor begins conducting. For simplicity and cost considerations, an inverse discrete Fourier transform (IDFT) [36] was chosen to approximately invert $I(\omega)$. To sufficiently minimize the effects of the IDFT approximation to the continuous inverse Fourier transform, a 1024 point transform with a sample time of 5 microseconds was chosen. This makes the folding frequency 100kHz, which is considerably above any significant frequencies measured in the spectrum of the current in the prototype EIDI system. The 200kHz frequency domain window of the IDFT is sufficiently large that "windowing" effect errors in the time domain response are not too great. (These errors are primarily manifested as Gibbs' ripples on the intitial current calculated in Section 6.3.3, described in Section 6.3.4 and shown in Figure 19.)

In order to determine how long a time this calculated current approximates the actual circuit current, a second calculation was performed using the circuit model in Figure 17. The model predicts a frequency domain voltage corresponding to the physical EIDI capacitor voltage of

$$V_c(\omega) = V_o\left[\pi\delta(\omega) + \frac{1}{j\omega}\right] - \frac{V_o\left[\pi\delta(\omega) + \frac{1}{j\omega}\right]\frac{1}{j\omega C}}{\frac{1}{j\omega C} + R(\omega) + j\omega L(\omega)}$$

$$V_c(\omega) = CV_o \frac{R(\omega) + j\omega L(\omega)}{1 - \omega^2 CL(\omega) + j\omega CR(\omega)} \quad (42)$$

The term involving the delta distribution again contributes nothing to the inverse Fourier integral yielding the time domain voltage, and is dropped from consideration to yield (42). A 1024 point 5 microsecond sample time IDFT was used to approximately calculate the inverse Fourier transform of (42). Output from the IDFT showed that the capacitor voltage would slew negatively through zero volts at t=279 microseconds. This is the time at which the diode across the capacitor is modeled as coming into conduction and acting as a short circuit. Beyond this time the model of Figure 17 is no longer valid, and consequently the current predicted by the model is no longer correct.

6.3.3 Current After Clamp Diode Conduction

Once the diode comes into conduction, the model of the EIDI circuit for all future time is as shown in Figure 18. The inductance and resis-

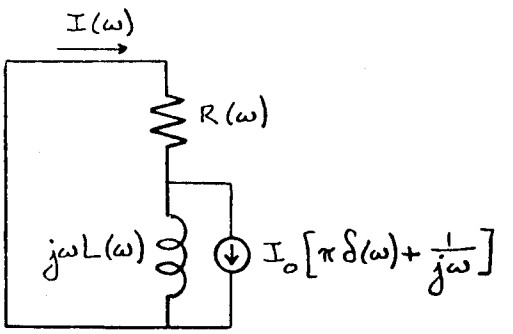

FIGURE 18
FREQUENCY DOMAIN CIRCUIT MODEL CLAMP DIODE ON

tance in this circuit have the same physical significance that they had in Figure 17, and their values are calculated for any desired frequency using the same algorithms. For computational convenience, time is "re-

set" to zero in this circuit, even though the circuit does not come into existance until t=279 microseconds in the Figure 17 circuit. Since the current in the coil is not initially zero, the circuit's magnetic energy storage at the new "t=0" is modeled by including a DC current source in parallel with a frequency dependent inductance. This current source is zero for all time prior to t=0, and for all future time has a D.C. value I_o equal to the value of the current in the Figure 17 circuit at the time the capacitor voltage became zero.

Current in the Figure 18 circuit is given in the frequency domain by

$$I(\omega) = I_o \left[\pi\delta(\omega) + \frac{1}{j\omega} \right] \frac{j\omega L(\omega)}{R(\omega) + j\omega L(\omega)}$$

$$I(\omega) = I_o \frac{L(\omega)}{R(\omega) + j\omega L(\omega)} \qquad (43)$$

Note that the term containing the delta distribution once again contributes nothing to the inverse Fourier transform of $I(\omega)$, and is dropped in (43). An IDFT was used to calculate the approximate inverse Fourier transform of $I(\omega)$ given in (43), in exactly the same manner that the expression for $I(\omega)$ in (42) was inverted. The program is very similar to the one used in the Section 6.3.2 current calculation.

6.3.4 Combining Pre- and Post Clamp Diode Conduction Current

Because of the presence of the current source in parallel with the inductor in Figure 18, the current in this circuit model is discontinuous at t=0. Consequently, the current cannot be bandlimited. An inherent assumption in the use of the discrete Fourier transform is that the signal is bandlimited. The time domain current calculated by the IDFT showed a small amount of ripple during the first 100 microseconds due to

the current spectrum not being bandlimited. Prior to "joining" in time the current predicted by the Figure 17 model with the current predicted by the Figure 18 model, this ripple was eliminated by graphically choosing current values lying close to the IDFT predicted values that joined smoothly with the current from the Figure 17 model. Figure 19 illustrates this procedure. Current ripple amplitude was 54 amps peak to peak at t=10 microseconds, decaying to 1 amp peak to peak at t=75 microseconds, with time measured in the Figure 18 model. Figure 20 shows how good the agreement is between this piecewise linear model predicted current and the current measured in the prototype EIDI circuit.

With the model predicted current now available at 5 microsecond intervals from t=0 to t=5.12 milliseconds, a 1024 point 5 microsecond sample time DFT was performed on the current samples to estimate the Fourier transform $I(\omega)$ of the model current. This transform is needed for use in calculating the magnetic induction fields from the Hankel space transmission line coil-target model, as discussed in the next section.

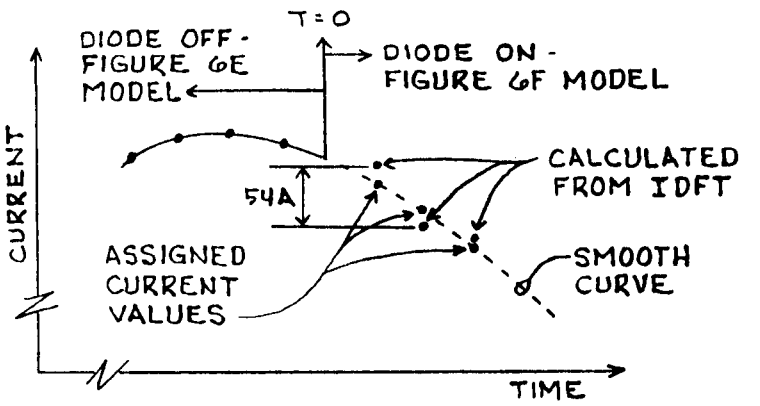

FIGURE 19
PRE- AND POST- CLAMP DIODE CONDUCTION CURRENT

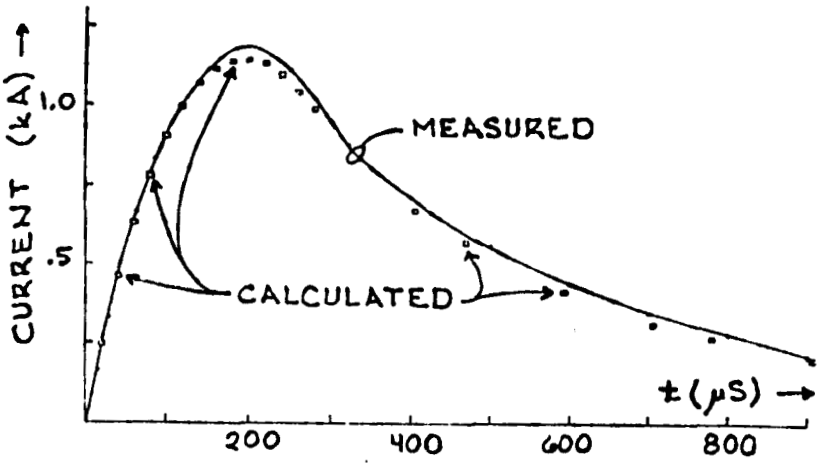

FIGURE 20
COIL CURRENT

6.4 MAGNETIC INDUCTION

6.4.1 Introduction

Knowledge of the radial and axial magnetic induction on the coil side face of the target is required for calculation of the total force on the target. Although conceptually simple, the numerical calculation of these two fields presented more computational difficulties than were encountered in the combined total of all other calculations performed. Initial attempts at calculating the magnetic induction, performed using single precision arithmetic and using professionally written quadrature routines, produced results that were incorrect by orders of magnitude.

6.4.2 Radial Magnetic Induction on the Coil Side Face of the Target

Expression (44) shows the iterated improper integral that is to be evaluated numerically to calculate the time domain radial magnetic induction $B_r(0,r,t)$. This integral is the inverse Fourier-Hankel transform of the total current at z=0 given by (25) of Chapter 4.

$$B_r(0,r,t) = \mu \int_{\omega=-\infty}^{\infty} e^{j\omega t} I(\omega) \times$$

$$\int_{\lambda=0}^{\infty} \frac{K'(\lambda)\, e^{-\lambda g}\left[1 + e^{-\frac{\lambda h}{3}} + e^{-\frac{2\lambda h}{3}}\right] J_1(\lambda r)\, \lambda \, d\lambda}{1 + \frac{1}{\sqrt{\lambda^2 + j\omega\mu\sigma}} \; \frac{1 + \frac{\lambda}{\sqrt{\lambda^2 + j\omega\mu\sigma}} \tanh(\gamma_m d)}{\frac{\lambda}{\sqrt{\lambda^2 + j\omega\mu\sigma}} + \tanh(\gamma_m d)}} \, d\omega \qquad (44)$$

Quadrature of iterated integrals is almost always difficult [21]. One of the most common methods of evaluating such integrals, the Monte Carlo method, could not even be considered for use in (44) due to the enormity of the very expensive and random complex function evaluations required by such an approach. Furthermore, the integrand in (44) is extremely oscillatory, having both positive and negative complex values, due to the Bessel function in the inverse Hankel transform, the function $K'(\lambda)$, and the complex exponential in the inverse Fourier transform. Quadrature of such integrands is all but impossible using Monte Carlo methods due to extreme smearing [25], [26]. It is the oscillatory nature of the integrand in (44) that makes its evaluation difficult.

After much trial and error, a workable approach to quadrature of the integral in (44) was obtained, and is described in this section. No claim is made for optimality or near optimality in this approach. After many computations of the magnetic induction had been performed using this procedure, it became apparent that simplifications could be made, while still obtaining sufficient accuracy. However, these simplifications have not been tested, and the original approach to quadrature of the integral in (44) will be described.

Measurements of the radial magnetic induction near the coil side face of the target in the EIDI prototype system provide some insight into a suitable numerical procedure for evaluating the integral in (44). The Fourier transforms of these observed fields are smooth (higher order derivatives with respect to frequency are small) with most of the energy confined to relatively low frequencies. This suggested the use of an IDFT to numerically perform the inverse Fourier transformation in (44). Further impetus for use of the IDFT is given by noting that the DFT procedure for calculating the Fourier transform $I(\omega)$ of the current, described in the preceding section, yielded transform values at equally spaced frequencies. These are the appropriate frequencies for calculating a 1024 point IDFT, with a 5 microsecond sample time, of the Fourier space radial magnetic induction. However, numerical evaluation of the inverse Hankel transform in (44) at the 513 frequencies needed for calculating a 1024 point IDFT yielding a real sequence is prohibitively expensive. This expense was avoided by using the previously noted fact that the expected Fourier transform of the magnetic induction is smooth, with most of the energy confined to low frequencies. Accordingly, the inverse Hankel transform in (44) was evaluated at only 77 frequencies, chosen to provide a reasonable representation of the behavior of the Fourier transform of the known radial magnetic induction. Spline function approximations were then fitted to the real and imaginary parts of the calculated inverse Hankel transforms. The IDFT routine to calculate the desired time domain magnetic induction uses these spline functions to form $B_r(0,r,\omega)$ at the 1024 frequencies needed.

With a procedure for evaluating the inverse Fourier integral in (44) available, a search for a suitable method for quadrature of the inverse

Hankel integral was initiated. The infinite upper limit of this integral was simply replaced with a suitably large finite upper limit, due to the controlling factor in the leading behavior of the asymptotic expansion of the integrand being $e^{-\lambda g}$. With the problem of the infinite upper limit gone, the remaining difficulties may be divided into two somewhat overlapping classes.

Selection of a suitable algorithm for performing the quadrature is essential if accurate results are to be obtained. Most of the common quadrature algorithms are incapable of dealing with oscillatory integrals without some help. Even with the best of help, examples of problems where these algorithms completely fail abound. This has given rise to highly specialized techniques for quadrature involving oscillatory integrands [27], [28], [29], [30]. The use of one of these specialized algorithms was avoided by writing a double precision Gaussian quadrature routine [21], [31]. This routine was then used to perform the inverse Hankel integration in (44) over the range $0 < \lambda < 10$, then over the range $10 < \lambda < 20$, etc., stopping when the desired upper limit of integration had been reached. The results of these integrations, which can be interpreted as terms in a sequence that are to be summed, were then added together first using straightforward addition, and then using the Euler series summation convergence acceleration algorithm DTEUL from the NASA Lewis Research Analysis Center Software Library [34]. For each radius at which the radial magnetic induction was evaluated, and for each of the 77 Fourier frequencies, good agreement was achieved between the results of these two summation methods.

Several different finite upper limits were used to take the place of the infinite upper limit in the inverse Hankel quadrature. It was

experimentally determined that upper limits greater than 1000 resulted in very little change in the calculated induction fields.

The second problem concerned the precision of the FORTRAN implemented on the IBM 370. Single precision floating point word length on the 370 is approximately 7 decimal digits (24 bit mantissa) [25]. This is insufficient for nearly all complex scientific calculations [32], [33]. Double precision floating point word length on the 370 is approximately 15 decimal digits (56 bit mantissa) [25], and was used for all computations involving the inverse Hankel integral. Without the use of double precision arithmetic, inverse Hankel quadrature was impossible due to smearing.

Although the use of double precision greatly reduced the effects of smearing, it created problems of its own. A double precision Bessel function, and a double precision algorithm for $K'(\lambda)$ become necessary to evaluate (44). Simply converting a single precision algorithm for $K'(\lambda)$ to double precision does not yield sufficient accuracy to obtain good results. Double precision Bessel function algorithms were unavailable at The Wichita State University. Double precision algorithms were written for $J_0(x)$ and $J_1(x)$. The double precision algorithm that was written for $K'(\lambda)$ is described in the Appendix. Figure 21 provides a comparison between the measured radial magnetic induction close to the coil side face of the target, and the predicted radial magnetic induction on the coil side face of the target.

6.4.3 Axial Magnetic Induction on the Coil Side Face of the Target

The magnetic induction B_z on the target next to the coil is calculated by performing an inverse Fourier transform on (36) in Section 4.4

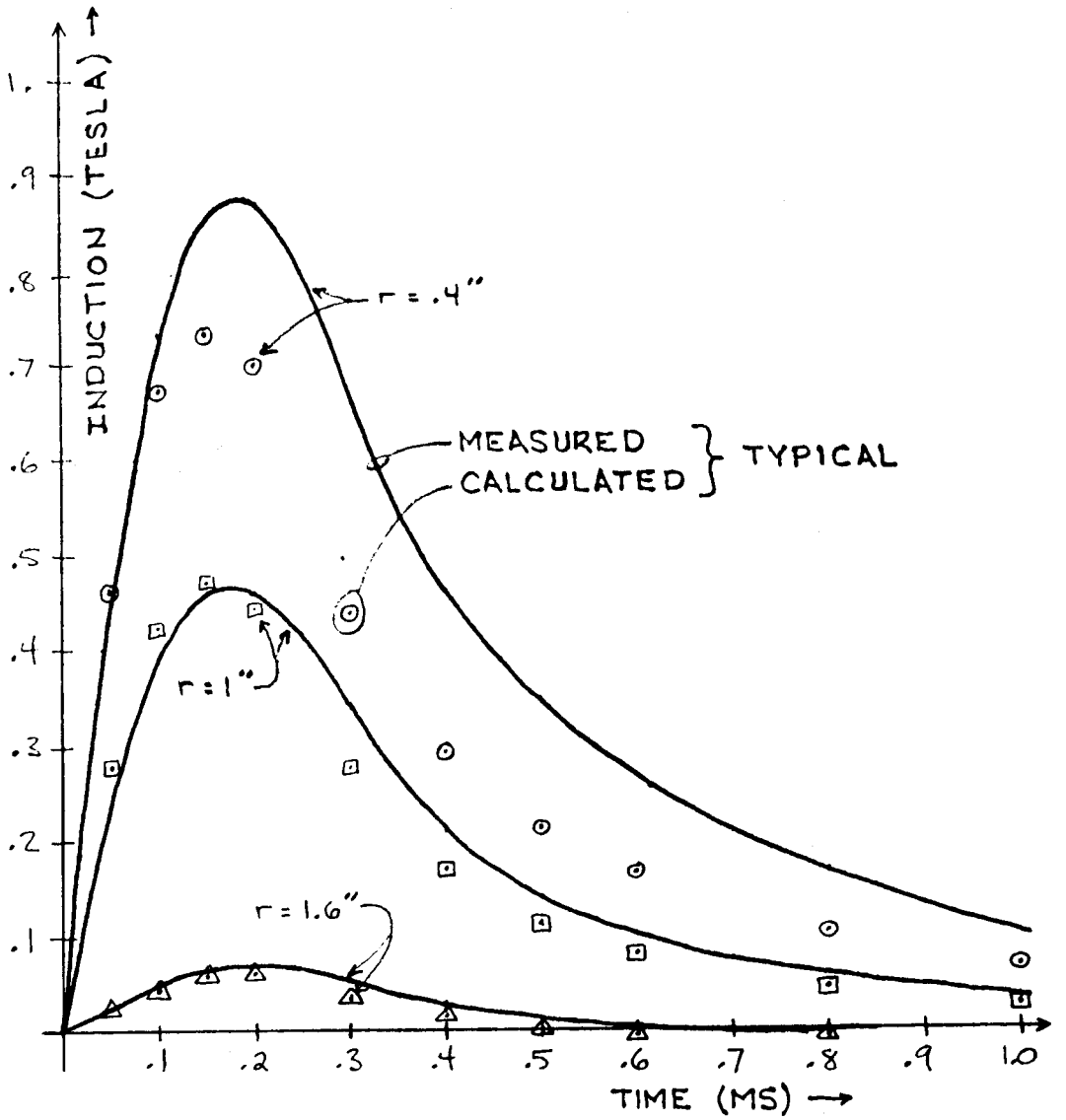

FIGURE 21
B_r VERSUS TIME
NEAR SIDE OF TARGET

of Chapter 4. Then

$$B_z(0,r,t) = \mu \mathcal{F}^{-1}\{H_z(0,r,t)\}$$

$$B_z(0,r,t) = \mu \mathcal{F}^{-1}\left\{ \frac{-1}{j\omega} \int_0^\infty V(0,\lambda,\omega)\, \lambda^2 J_0(\lambda r)\, d\lambda \right\}$$

where $V(0,\lambda,\omega)$ is given by (30) in Section 4.3.1 of Chapter 4. Substituting (30) into the above,

$$B_z(0,r,t) = -\mu \int_{\omega=-\infty}^{\infty} e^{j\omega t}\, I(\omega) \quad \times$$

$$\int_{\lambda=0}^{\infty} \frac{K'(\lambda)\mu\lambda\, e^{-\lambda g}\left(1 + e^{-\frac{\lambda h}{3}} + e^{-\frac{2\lambda h}{3}}\right) J_0(\lambda r)\, d\lambda}{1 + \frac{\sqrt{\lambda^2 + j\omega\mu\sigma}}{\lambda} \dfrac{\dfrac{\sqrt{\lambda^2 + j\omega\mu\sigma}}{\lambda} + \tanh(\gamma_m d)}{1 + \dfrac{\sqrt{\lambda^2 + j\omega\mu\sigma}}{\lambda}\tanh(\gamma_m d)}}\, d\omega \qquad (45)$$

The similarity between (44) and (45) is evident, even though the order of the inverse Hankel transforms is different. Because of this similarity, the algorithms developed to perform the quadrature in (44) were used, with only evident minor changes necessary, to perform the quadrature in (45). A comparison at several different radii between the measured axial magnetic induction close to the coil side face of the target and the calculated axial magnetic induction on the surface of the target closest to the coil is shown in Figure 22.

6.4.4 Magnetic Induction on the Opposite Face of the Target

Although it was not needed in the calculation of the force between the coil and target, the magnetic induction on the side of the target

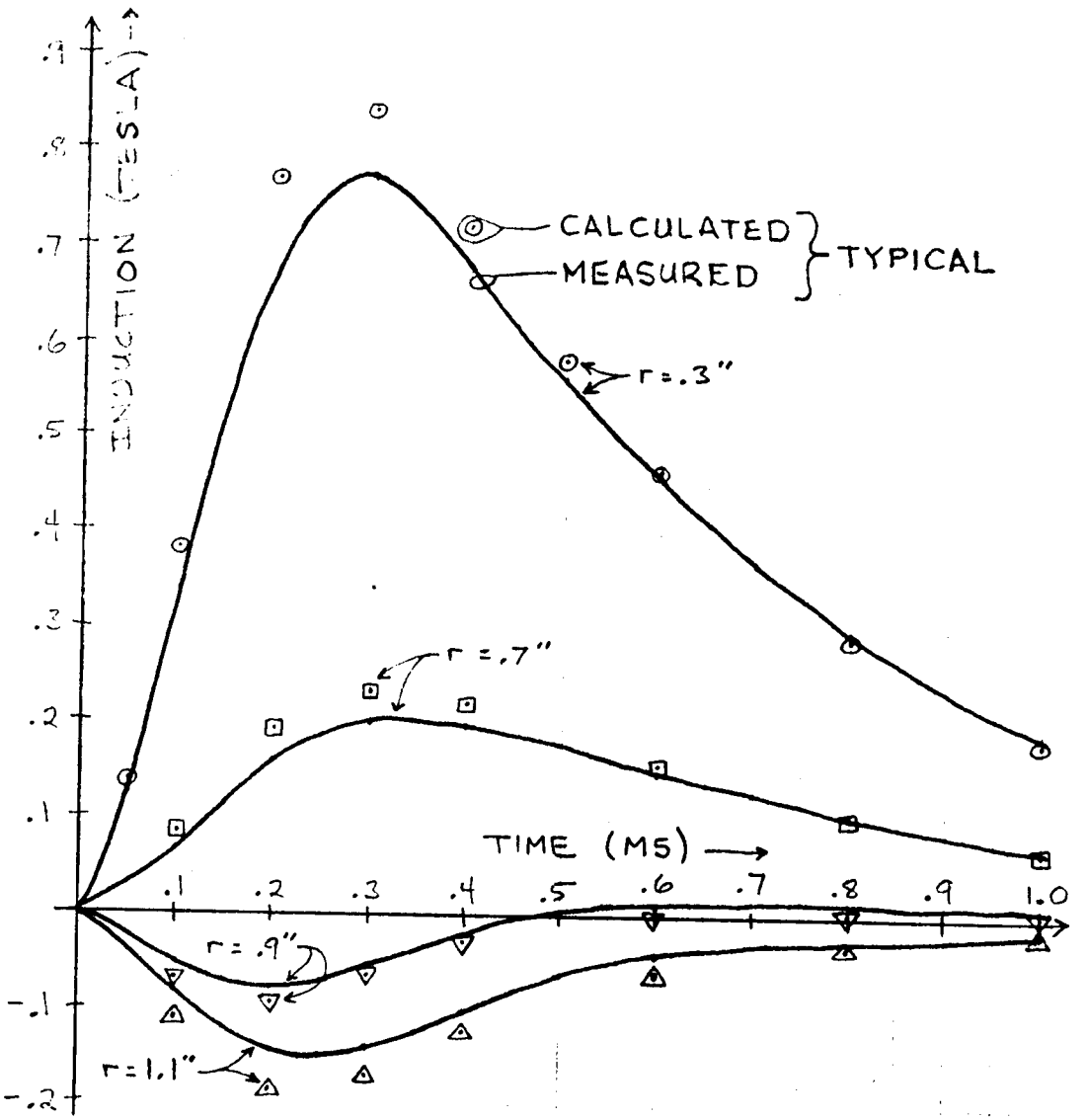

FIGURE 22
B_Z VERSUS TIME
NEAR SIDE OF TARGET

away from the coil was calculated for comparison with the measured induction close to the same target surface. Section 4.3 in Chapter 4 derived expressions for the total voltage V_f and total current I_f at the junction between the metal line and air line opposite the current sources. These quantities correspond respectively to the azimuthal electric intensity and the radial magnetic induction on the surface of the target opposite the coil.

Inverse Fourier-Hankel transformation similar to that in (44), but with the integrand corresponding to the current I_f given in Section 4.3, yields the radial magnetic induction. Only minor changes are necessary in the FORTRAN program to calculate the induction. Figure 23 provides a comparison between the measured and calculated radial magnetic induction close to and on the target surface away from the coil.

Inverse Fourier-Hankel transformation similar to that in (45), but with the integrand corresponding to the voltage V_f given in Section 4.3, yields the axial magnetic induction. Figure 24 shows the comparison between the measured and calculated axial induction close to and on the target surface away from the coil.

6.5 FORCE VERSUS TIME

It was shown in Section 4.5 of Chapter 4 that the total force between the coil and target is given approximately by

$$F_z(t) \doteq \frac{\pi}{\mu} \int_0^\infty [B_z^2(o,r,t) - B_r^2(o,r,t)]\, r\, dr \qquad (46)$$

For use in this integral, radial magnetic induction was calculated at 5 microsecond intervals at radii .01", .2", and in .2" increments up to a maximum of 2.0", on the surface of the target closest to the coil using

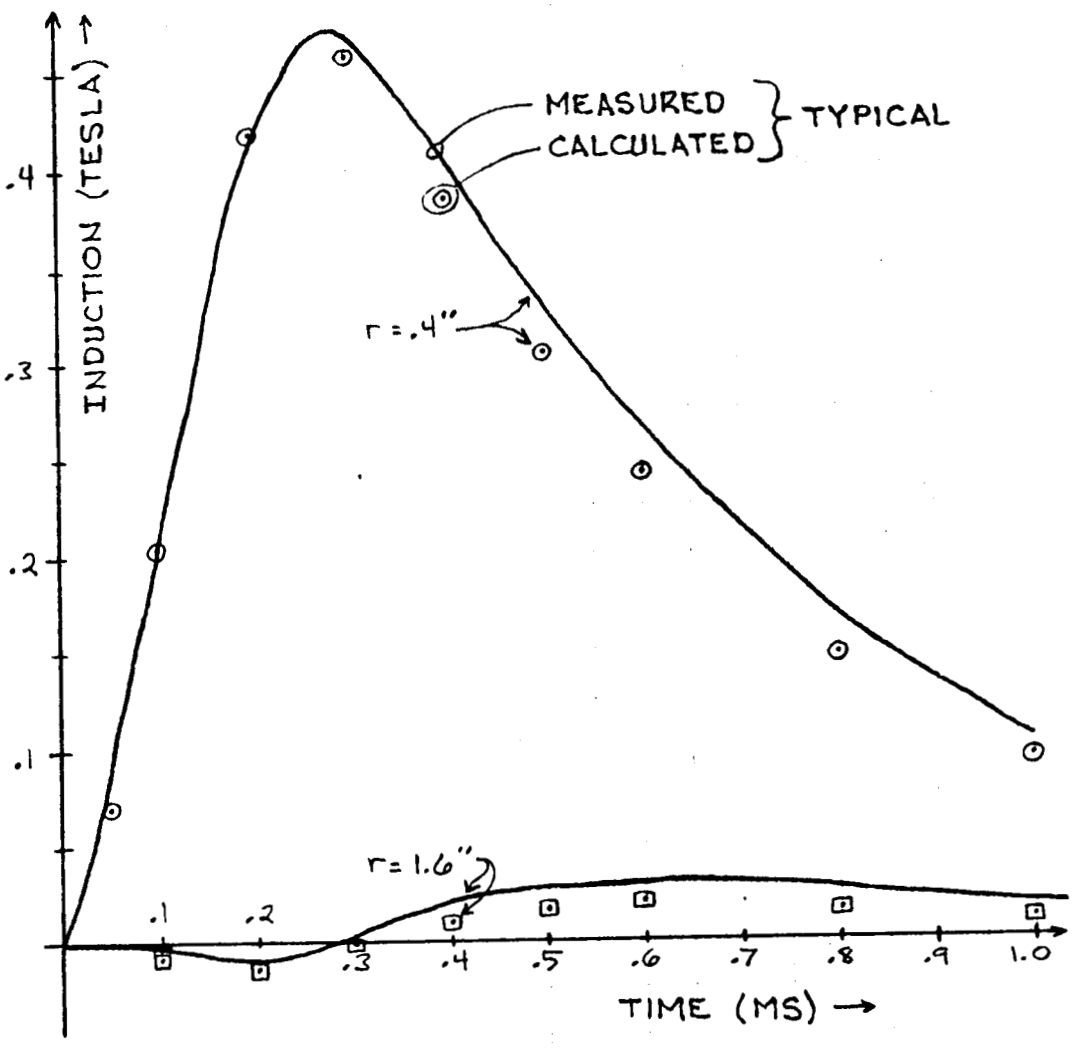

FIGURE 23
B_r VERSUS TIME
FAR SIDE OF TARGET

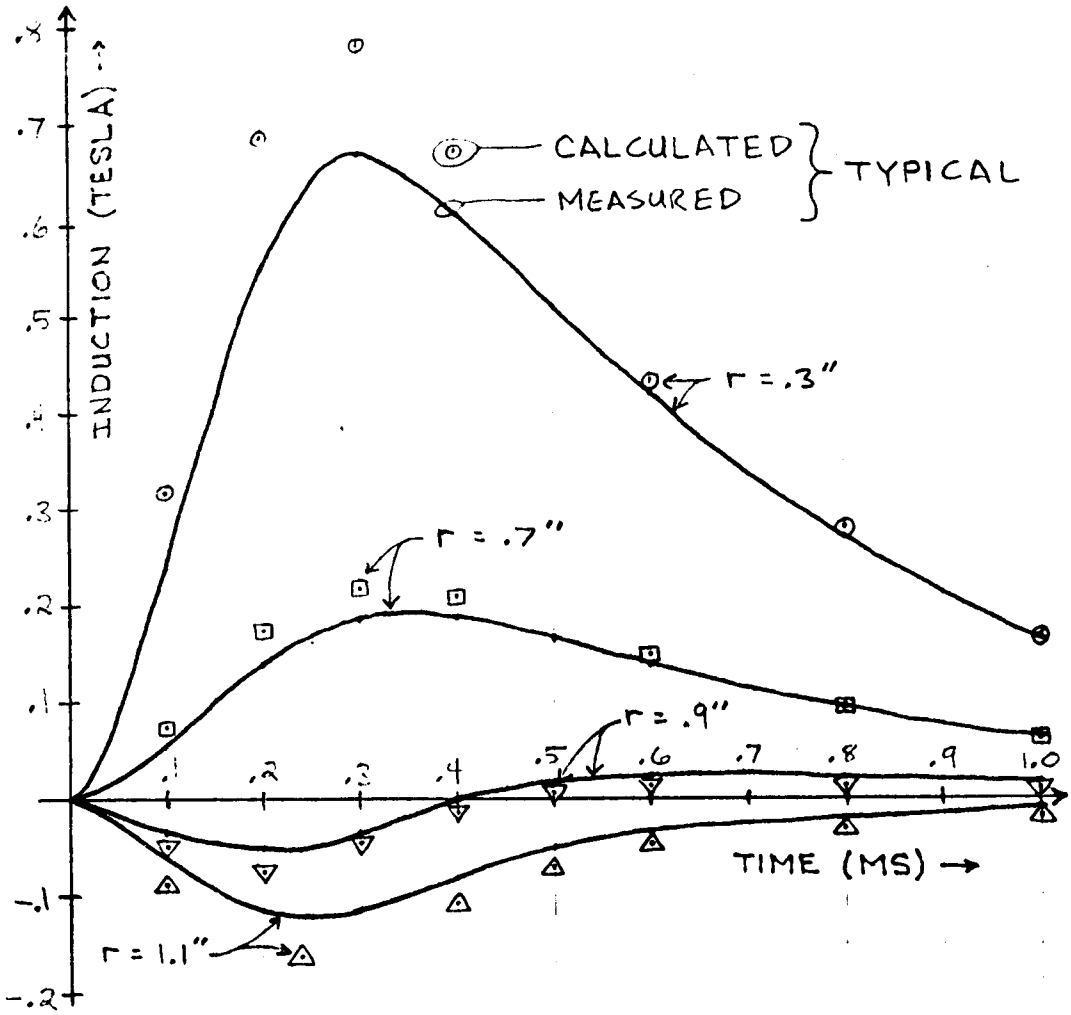

FIGURE 24
B_Z VERSUS TIME
FAR SIDE OF TARGET

the algorithms described in Section 6.4.2. Axial magnetic induction was also calculated at 5 microsecond intervals at radii .01", .1", and in .2" increments up to 1.9", on the same target surface using the algorithms described in Section 6.4.3. Cubic spline functions were then fitted to the squares of the radial variation of these two magnetic fields at times 0, 50, 100, 150, ..., 900, and 1125, 1400, and 2000 microseconds for use in performing the quadrature indicated in (36), using an upper limit of 1.9". The quadrature was done exactly (to the limit of the machine arithmetic) on the spline function approximations to the squared fields by integrating the cubic polynomial form of the spline function between knots, and using the spline function coefficients in the result.

Figure 25 shows the force versus time calculated using this procedure.

6.6 IMPULSE

Equation (39) in Chapter 4, repeated below, was used to calculate

$$\Gamma = \int_0^\infty F_z(t)\, dt$$

the impulse delivered to the target by the coil. A spline function was fitted, with time as the variable, to the force calculated in Section 6.5 above. An exact integration was performed on the cubic polynomials of the spline function between knots, with the result that the impulse calculated was .008 lb-sec. This is lower than the .012 lb-sec impulse measured using a ballistic pendulum. It should be noted that the quadrature of the force integral in (46) above used an upper limit of r=1.9" instead of infinity. Although the induction decays as the radius tends to infinity, an unknown part of the force has been ignored by not taking the induction fields at radii greater than 1.9" into account.

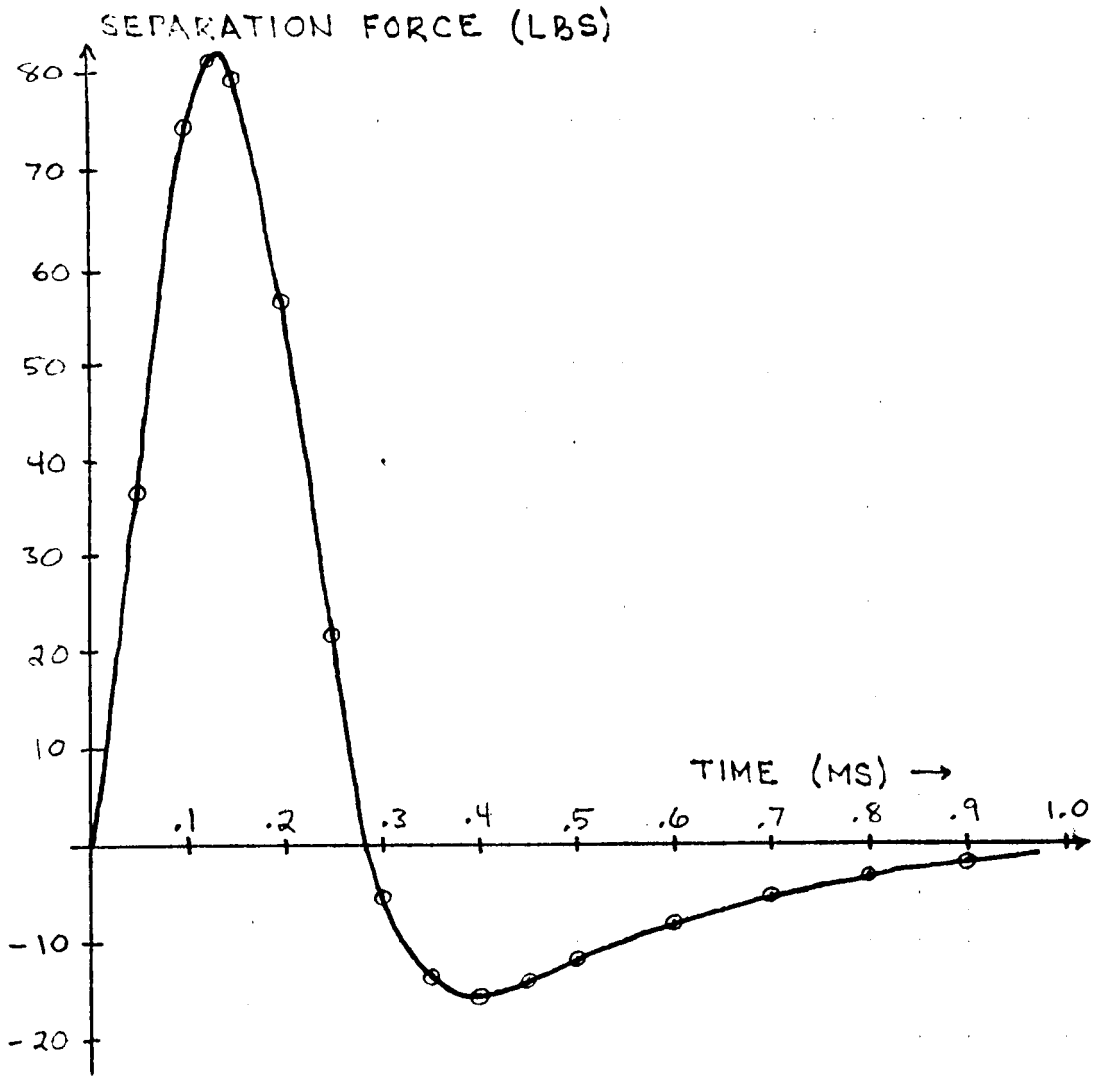

FIGURE 25
FORCE BETWEEN COIL AND TARGET

CHAPTER SEVEN

CONCLUSION AND RECOMMENDATIONS FOR FURTHER WORK

7.1 CONCLUSION

7.1.1 Summary

A method of modeling the electrical system aspects of a coil and metal target configuration resembling a practical Electro-Impulse De-Icing installation, and a simple circuit for providing energy to the coil, was presented. The model was developed in sufficient theoretical detail to allow the generation of computer algorithms for the current in the coil, the magnetic induction on both surfaces of the target, the force between the coil and target, and the impulse delivered to the target. These algorithms were applied to a specific prototype EIDI test system for which the current, magnetic fields near the target surfaces, and impulse had previously been measured.

Coil impedance was the first quantity calculated using the algorithms. Agreement between the impedance calculated and the impedance measured was seen to be very good for the resistive part, and reasonable for the reactive part. Despite the simple model used for the circuit providing energy to the coil, excellent agreement was obtained between the predicted and measured coil current.

Measured and predicted magnetic induction fields were not directly compared, due to the fields having been measured close to, but not on, the target surfaces using spatial averaging methods. The only fields calculated were on the target surfaces, for use in calculation of the force between the coil and target. Nevertheless, there was seen to be

very reasonable agreement between measured and calculated magnetic fields. The character of the time variation of these fields changed considerably with radial distance from the axis, and the algorithms correctly predicted these changes.

Calculation of the impulse easily provided the greatest disagreement between a predicted and measured quantity, with a -33% error in the calculated impulse. Impulse was measured using a ballistic pendulum containing the metal target, so, for this measurement, the metal target was no longer held rigid when the capacitor was discharged through the coil. This does not satisfy the model assumption of a stationary system. However, the period of the pendulum was sufficiently long that, during the time interval when most of the force was developed on the target, negligible motion of the pendulum should theoretically have occured. Motion of the target during the measurement of the impulse is not felt to be a satisfactory explanation for the discrepancy between the measured and calculated impulse. It was mentioned in Section 6.6, where the calculation of the impulse was described, that the infinite upper limit in the integral yielding the theoretical impulse had been replaced with a finite upper limit for the purpose of quadrature, thus incurring an unknown error. This procedure for quadrature of the impulse integral is felt to be the most likely source of error in the calculated impulse.

7.1.2 Original Contributions

Reference [4] provided most of the basic methods used in this report in modeling the interaction between the coil and target. It was shown that an error had occured in the definition given in [4] of the characteristic impedance of a Hankel space transmission line, and the corrected

definition was used in the theoretical development of the model. For many transmission line calculations, this error does not become evident because impedances occur in ratios (e.g., the voltage and current reflection coefficient calculations in Section 4.3.1).

Reference [4] provided no method of calculating the axial magnetic induction $B_z(z,r,t)$ from the transmission line model. An integral solution for this field, in terms of the transmission line voltage, was derived in Section 4.4. This solution allowed the use of nearly all of the algorithms developed for the calculation of the radial magnetic induction $B_r(z,r,t)$ in calculating the axial magnetic induction $B_z(z,r,t)$.

The most significant contribution of this work was the development of FORTRAN algorithms for performing the inverse Fourier-Hankel transformations yielding the induction fields, described in Section 6.4. While there were no theoretical contributions made during the development of these algorithms, several diverse results from the fields of numerical analysis and approximation theory had to be applied in concert to create a working algorithm. During this development, an algorithm for the generation of Struve functions of the first and second orders was developed that, according to a computer search of the literature, is the most accurate reported.

7.2 RECOMMENDATIONS FOR FUTURE WORK

If the methods developed in this report are to be applicable as design tools for EIDI systems, the algorithms for the calculation of the magnetic induction fields should be made more efficient. These algorithms take nearly half an hour of CPU time on the IBM 370 to calculate either the axial or the radial magnetic induction versus time at one

specific radius. Both the radial and axial components are required, each at eleven different radii, for the force calculation described in Section 6.5. A minimum of eleven hours of CPU time is too great for the evaluation of the force-time profile of a proposed EIDI configuration. The least desirable feature of the methods presented in this report is the inordinate CPU time required for the calculation of the induction fields. A sophisticated convergence acceleration routine could perhaps be devised specifically for more economic calculation of the induction fields.

Human intervention is required to proceed along the Analysis Flow Diagram of Figure 1 (page 4) in evaluating a specific EIDI system. This is because the outputs from the various programs, represented by such Figure 1 quantities as the coil impedance $Z(\omega)$, the current $i(t)$ and $I(\omega)$, are not in the form required as the inputs for the program at the next block in Figure 1. A significant amount of design automation could be accomplished by writing one long program, using as a skeleton the programs developed for this report, that will take as input the geometry of the coil-target configuration and the circuit used to provide energy to the coil, and provide as output a force-time profile and the total impulse delivered to the target.

Not all possibilities have been exhausted in the search for an analytical (or semianalytical) solution to the EIDI design problem. Perturbation techniques have been suggested as a possible method for analytical Hankel inversion in the calculation of the magnetic induction, and should be investigated, as this is the area suffering the greatest computational expense. Furthermore, analytical solutions (if sufficiently simple) are often capable of providing insight into a problem not provided by numerical solutions.

APPENDIX

CALCULATION OF $K'(\lambda)$

The function $K'(\lambda)$ arises from the transformation of real space current discs into Hankel space. Using N=30 turns (the number of turns of the coil in the experiment described in Chapter 5) in the expression for $K'(\lambda)$ on the top of page 24 yields

$$K'(\lambda) = \frac{30}{3(R_2 - R_1)} \int_{R_1}^{R_2} x \, J_1(\lambda x) \, dx \qquad (47)$$

Straightforward quadrature of (47) using the Newton-Cotes algorithm QUANC8 was initially performed for generating values of $K'(\lambda)$ for use in approximating $K'(\lambda)$ with a cubic spline function. This provided sufficient accuracy for use in numerical calculation of coil impedance as described in Section 6.2. Attempts at calculating the radial magnetic induction B_r using this spline function approximation for $K'(\lambda)$ were a total failure. This appendix describes a procedure for calculating $K'(\lambda)$ that is accurate to 13 digits when implemented in double precision FORTRAN on an IBM 370.

The integral in (47) can be evaluated in closed form in terms of named special functions. Change variables,

$$\lambda x = y \quad \Rightarrow \quad dx = dy/\lambda$$

$$x = R_1 \quad \Rightarrow \quad y = \lambda R_1$$

$$x = R_2 \quad \Rightarrow \quad y = \lambda R_2$$

so that (47) becomes

$$K'(\lambda) = \frac{10}{R_2 - R_1} \int_{\lambda R_1}^{\lambda R_2} \frac{y}{\lambda} J_1(y) \frac{dy}{\lambda}$$

$$K'(\lambda) = \frac{10}{R_2 - R_1} \frac{1}{\lambda^2} \int_{\lambda R_1}^{\lambda R_2} y J_1(y)\, dy \qquad (48)$$

From reference [18],

$$\int J_1(y)\, y\, dy = \frac{\pi y}{2} \left[J_1(y) H_0(y) - H_1(y) J_0(y) \right]$$

where $H_0(x)$ and $H_1(x)$ are Struve functions of orders 0 and 1 respectively [18], [19], and $J_0(x)$ and $J_1(x)$ are Bessel functions of the first kind of orders 0 and 1 respectively. Using this result in (48) yields

$$K'(\lambda) = \frac{5\pi y}{\lambda^2 (R_2 - R_1)} \left[J_1(y) H_0(y) - H_1(y) J_0(y) \right] \Big|_{y = \lambda R_1}^{\lambda R_2} \qquad (49)$$

In order to use this result, double precision algorithms for generating the Bessel and Struve functions must be available. Double precision Bessel functions are readily available, but Struve functions are not. A computer search of the literature resulted in a reference to a Naval Research Laboratory report that contained FORTRAN source code for generating integer order Struve functions with positive arguments [36]. This code could not be used because it used subroutines to which access was not readily available.

For several years, mathematicians have been aware of the desirability of using truncated Jacobi series of Chebyshev polynomials for numerical approximation of various special functions [37], [38]. Luke [37] provides coefficients b_n and c_n for Chebyshev series expansions

$$H_0(x) = \frac{x}{8} \sum_{n=0}^{\infty} b_n T_{2n}\left(\frac{x}{8}\right), \qquad |x| \le 8$$

$$H_1(x) = \sum_{n=0}^{\infty} c_n T_{2n}\left(\frac{x}{8}\right), \qquad |x| \le 8$$

where $T_{2n}(x)$ is a Chebyshev polynomial of the first kind of order 2n. All coefficients having magnitudes greater than 10^{-20} are given, allowing

generation of $H_0(x)$ and $H_1(x)$ with 20 decimal digit accuracy for arguments whose magnitude is less than 8 [39]. Using the identity

$$T_{2n}(x) = T_n(2x^2 - 1)$$

and retaining sufficient terms for 15 digit accuracy, these series expansions become

$$H_0(x) \doteq \frac{x}{8} \sum_{n=0}^{14} b_n T_n\left[2\left(\frac{x}{8}\right)^2 - 1\right], \quad |x| \le 8 \tag{50}$$

$$H_1(x) \doteq \sum_{n=0}^{14} c_n T_n\left[2\left(\frac{x}{8}\right)^2 - 1\right], \quad |x| \le 8 \tag{51}$$

Then for arguments λ such that $\lambda R_1 < 8$, the expression on the right hand side of (49) is evaluated using (50) and (51). Chebyshev polynomials are evaluated in double precision arithmetic using the subroutine DCNPS from the NASA Lewis Research Analysis Center Software Library [40].

Luke also lists coefficients d_n and e_n for the series

$$H_0(x) - Y_0(x) \doteq \frac{2}{\pi x} \sum_{n=0}^{19} d_n T_{2n}\left(\frac{8}{x}\right), \quad |x| \ge 8$$

$$H_1(x) - Y_1(x) \doteq \frac{2}{\pi} \sum_{n=0}^{16} e_n T_{2n}\left(\frac{8}{x}\right), \quad |x| \ge 8$$

for 15 digit accuracy. The functions $Y_0(x)$ and $Y_1(x)$ are Bessel functions of the second kind of orders 0 and 1 respectively. Rather than use these series directly to evaluate $H_0(x)$ and $H_1(x)$ for arguments greater than 8, some simplification is possible. Writing

$$H_0(x) \doteq \frac{2}{\pi x} \sum_{n=0}^{19} d_n T_{2n}\left(\frac{8}{x}\right) + Y_0(x) \triangleq A_0(x) + Y_0(x)$$

$$H_1(x) \doteq \frac{2}{\pi} \sum_{n=0}^{16} e_n T_{2n}\left(\frac{8}{x}\right) + Y_1(x) \triangleq A_1(x) + Y_1(x)$$

and substituting these expressions for $H_0(x)$ and $H_1(x)$ into the expres-

sion $J_1(x)H_0(x) - H_1(x)J_0(x)$ appearing in (49),

$$J_1(x)\,H_0(x) - H_1(x)\,J_0(x) = J_1(x)[A_0(x) + Y_0(x)] - [A_1(x) + Y_1(x)]\,J_0(x)$$

$$= J_1(x)\,A_0(x) - A_1(x)\,J_0(x) + J_1(x)\,Y_0(x) - Y_1(x)\,J_0(x)$$

$$= J_1(x)\,A_0(x) - A_1(x)\,J_0(x) + \frac{2}{\pi x}$$

using a well known property of the Wronskian of Bessel functions of the first and second kinds [18]. Thus, the expression on the right hand side of (49) can be written as

$$\frac{5\pi y}{\lambda^2(R_2 - R_1)}\left[J_1(y)\,A_0(y) - A_1(y)\,J_0(y) + \frac{2}{\pi y}\right]$$

when it is to be evaluated at an argument $y = \lambda R_n > 8$.

Using these results, $K'(\lambda)$ can be evaluated from (49) for non-negative values of the argument to at least 13 digit accuracy.

REFERENCES

[1] R.D. Rudich, "Weather-Involved U.S. Air Carrier Accidents 1962 - 1984 A Compendium and Brief Summary", American Institute of Aeronautics and Astronautics paper number AIAA-86-0327, January, 1986.

[2] British Patent Specification No. 505,433 issued to Rudolf Goldschmidt; May 5, 1939.

[3] Dr. Robert Schrag, unpublished paper, "Experimental Study of the Electro-Impulse Process by Magnetic Field Diagnostics", summarized in NASA CR 174919, May, 1985.

[4] M.H.S. El-Markabi and E.M. Freeman, "Electromagnetic Properties of a Circular Cylindrical Coil in a Set of Planar Ferromagnetic Regions", IEE Proc., Vol. 129, Pt. A, No. 8, Nov., 1982.

[5] General Electric Co., SCR Manual - Fifth Edition, Syracuse Park, N.Y., 1972.

[6] Richard G. Hoft, ed., SCR Applications Handbook, International Rectifier Corp., El Segundo, Ca., 1977.

[7] RCA Solid State Division, Solid State Devices Manual, Somerville, N.J., 1975.

[8] Samuel Levy, "Electromagnetic Shielding Effect of an Infinite Plane Conducting Sheet Placed Between Circular Coaxial Coils", Proceedings of the Institute of Radio Engineers, Vol. 24, No. 6, June, 1936.

[9] F.W. Grover, Inductance Calculations - Working Formulae and Tables, Dover, 1962.

[10] C.V. Dodd and W.E. Deeds, "Analytical Solutions to Eddy-Current Probe-Coil Problems", Journal of Applied Physics, Vol. 39, No. 6, May, 1968.

[11] M. Onoe, "Analysis of Finite Solenoid Coil Near a Conductor", Electr. Eng. Jpn., 88, 1968.

[12] Ian W. Sneddon, The Use of Integral Transforms, McGraw Hill Book Co., 1972.

[13] Robert A. Chipman, Transmission Lines, McGraw Hill Book Co., 1968.

[14] Robert Grover Brown, Robert A. Sharpe, William Lewis Hughes, and Robert E. Post, Lines, Waves, and Antennas: The Transmission of Electric Energy, 2nd. ed., Ronald Press, 1973.

[15] Richard E. Matick, Transmission Lines for Digital and Communication Networks, McGraw Hill Book Co., 1969.

[16] F.B. Hildebrand, Advanced Calculus for Applications, 2nd. ed., Prentice Hall, 1976.

[17] Murray R. Spiegel, Mathematical Handbook of Formulas and Tables, McGraw Hill Book Co., 1968.

[18] Arthur Erdelyi, ed., Higher Transcendental Functions, Vol. II, Bateman Manuscript Project, McGraw Hill Book Co., 1953.

[19] G.N. Watson, A Treatise on the Theory of Bessel Functions, 2nd. ed., Cambridge University Press, 1980.

[20] Milton Abramowitz and Irene A. Stegun, Handbook of Mathematical Functions with Formulas, Graphs, and Mathematical Tables, Dover Publications Inc., 1965.

[21] Robert W. Hornbeck, Numerical Methods, Prentice Hall, 1975.

[22] ACM Algorithms Distribution Service, IMSL Inc., Sixth Floor, NBC Building, 7500 Bellaire Boulevard, Houston, Texas, 77036.

[23] International Mathematical and Statistical Library (IMSL) Inc., Sixth Floor, NBC Building, 7500 Bellaire Boulevard, Houston, Texas, 77036.

[24] John R. Rice, Numerical Methods, Software, and Analysis, McGraw Hill Book Co., 1983.

[25] George E. Forsythe, Michael A. Malcolm, and Cleve B. Moler, Computer Methods for Mathematical Computations, Prentice Hall, 1977.

[26] Peter Henrici, Essentials of Numerical Analysis, John Wiley and Sons, 1982.

[27] Avram Sidi, "Extrapolation Methods for Oscillatory Infinite Integrals", Journal of the Institute of Mathematics and its Applications, vol. 26, 1980.

[28] David Levin and Avram Sidi, "Two New Classes of Nonlinear Transformations for Accelerating the Convergence of Infinite Integrals and Series", Applied Mathematics and Computation, Vol. 9, 1981.

[29] Avram Sidi, "The Numerical Evaluation of Very Oscillatory Infinite Integrals by Extrapolation", Mathematics of Computation, vol. 38, no. 158, April 1982.

[30] William F. Ford and Avram Sidi, "An Algorithm for a Generalization of the Richardson Extrapolation Process" (to be published).

[31] A.H. Stroud and D. Secrest, Gaussian Quadrature Formulas, Prentice

Hall, 1966.

[32] Personal conversation with Dr. Avram Sidi, The Technion, Israel Institute of Technology, Haifa, Israel.

[33] J.H. Wilkinson, Rounding Errors in Algebraic Processes, Prentice Hall, 1963.

[34] Frances B. Hildebrand, Introduction to Numerical Analysis, 2nd. ed., McGraw Hill Book Co., 1974.

[35] Mark Jong, Methods of Discrete Signal and System Analysis, McGraw Hill Book Co., 1982.

[36] Janet P. Mason, A Fortran Subroutine to Evaluate Struve Functions for Integer Orders and Positive Real Arguments, NRL Memorandum Report 3181, Research Computation Center, Naval Research Laboratory, Washington, D.C., December 1975.

[37] Yudell Luke, The Special Functions and their Approximations, Vol. II, Mathematics in Science and Endineering, Vol. 53-II, Academic Press, 1969.

[38] Cornelius Lanczos, Applied Analysis, Prentice Hall, 1956.

[39] C.W. Clenshaw, Mathematical Tables, Vol. 5, Chebyshev Series for Mathematical Functions, Her Majesty's Stationery Office, London, 1962.

[40] John F. Hart et. al., Computer Approximations, John Wiley and Sons, 1968.

[41] J.A. Stratton, Electromagnetic Theory, McGraw Hill Book Co., 1941.

[42] R.L. Schrag and G.W. Zumwalt, "Electro-Impulse Deicing: Concept and Electrodynamic Studies", American Institute of Aeronautics and Astronautics paper number 84-0021, January, 1984.

[43] R.M. Bowley, P.J. King, G.J. Lewis, and I.J. Shellard, "Production of Short Mechanical Impulses by Means of Eddy Currents", Proc. IEE, Vol. 130, Pt. B, No. 6, November 1983.

[44] G.J. Lewis, "The Electrodynamic Operation of Electro-Impulse De-Icing Systems", American Institute of Aeronautics and Astronautics paper AIAA-86-0547, January, 1986.

NASA
National Aeronautics and Space Administration

Report Documentation Page

1. Report No.	2. Government Accession No.	3. Recipient's Catalog No.
NASA CR-180845		

4. Title and Subtitle	5. Report Date
Theoretical Analysis of the Electrical Aspects of the Basic Electro-Impulse Problem in Aircraft De-Icing Applications	November 1987
	6. Performing Organization Code

7. Author(s)	8. Performing Organization Report No.
Robert A. Henderson and Robert L. Schrag	None
	10. Work Unit No. 505-68-11

9. Performing Organization Name and Address	11. Contract or Grant No.
Wichita State University College of Engineering Wichita, Kansas 67208	NAG3-284
	13. Type of Report and Period Covered Contractor Report Final

12. Sponsoring Agency Name and Address	14. Sponsoring Agency Code
National Aeronautics and Space Administration Lewis Research Center Cleveland, Ohio 44135-3191	

15. Supplementary Notes

Project Managers, John J. Reinmann and Robert J. Shaw, Propulsion Systems Division, NASA Lewis Research Center.

16. Abstract

A method of modeling a system consisting of a cylindrical coil with its axis perpendicular to a metal plate of finite thickness, and a simple electrical circuit for producing a transient current in the coil, is discussed in the context of using such a system for de-icing aircraft surfaces. A transmission line model of the coil and metal plate is developed as the heart of the system model. It is shown that this transmission line model is central to calculation of the coil impedance, the coil current, the magnetic fields established on the surfaces of the metal plate, and the resultant total force between the coil and plate. FORTRAN algorithms were developed for numerical calculation of each of these quantities, and the algorithms were applied to an experimental prototype system in which these quantities had been measured. Good agreement is seen to exist between the predicted and measured results.

17. Key Words (Suggested by Author(s))	18. Distribution Statement
Aircraft safety; Ice protection; Electromagnetic impulse deicer; Electrodynamic analysis	Unclassified - Unlimited Subject Category 03

19. Security Classif. (of this report)	20. Security Classif. (of this page)	21. No of pages	22. Price*
Unclassified	Unclassified	79	A05

*For sale by the National Technical Information Service, Springfield, Virginia 22161